Utrecht University

Thesis

To obtain the degree of Master of Science

# Interferometric Illumination Ptychography

*Author:*
Nicolaas van der Voort

*Supervisor:*
Dr. Stefan Witte

July 20, 2016


**Abstract**

A computational lensless phase microscope based on coherent diffraction is developed. Phase imaging with a pixel size limited resolution of 2.2 $\mu m$ is achieved without the need for assumptions about the object or mechanically moving parts. Several diffraction patterns are recorded using an illumination pattern caused by coherent interference of two beams. This type of image reconstruction using multiple illumination patterns is called ptychography.

# Contents

# Chapter 1

# Introduction

Coherent diffractive imaging (CDI) is a collection of imaging techniques that measure coherent diffraction patterns and use computational techniques to reconstruct images. Interest in CDI is driven by the increasing availability of coherent light sources in the EUV and X-ray wavelength ranges made possible by free electron laser (FEL) [1] and higher harmonics generation (HHG) [2]. For these short wavelength the limited quality of imaging optics creates a serious complication for any imaging technique that uses optics. CDI is inherently lensless and therefore it shows great potential to be combined with coherent short-wavelength sources to create a resolution in the several nanometre regime. Object reconstruction in CDI requires phase information. However detectors are only sensitive for the intensity of the incoming electromagnetic light field. Therefore all CDI techniques require some kind of phase retrieval. Ptychography is an implementation of CDI that varies the illumination pattern to create constraints such that the phase can be determined.

Phase retrieval from diffraction data was first demonstrated by Fienup in 1978 [3] who adapted an algorithm developed by Gerchberg and Saxton from 1972 [4] aimed at electron microscopy image retrieval. Phase retrieval algorithms have been further developed by Fienup in 1986 [5, 6] and Sheppard in 1999 [7]. Rodenburg in 2004 [8–10] made an adaption specific to ptychography with a scanning aperture. The feasibility of X-ray diffraction imaging was first shown in 1999 by Miao [11] who imaged gold particles in transmission. In 2001 Robinson [12] demonstrated the technique in a reflection geometry. A yeast cell was first imaged in 2005 by Shapiro [13]. Witte [14] demonstrated in 2014 diffraction imaging using broadband sources allowing for efficient use of luminosity. Other multi-wavelength techniques have been published by Noom and Witte [15]. Rodenburg [16] demonstrated in 2007 the use of a scanning aperture to perform X-ray ptychography imaging. A scanning aperture can be used to illuminate all areas at least twice such that sufficient information is present for phase retrieval. Assumptions on the

object can be made so supplement information for reconstruction available from diffraction measurements. However, this is often undesirable as not all objects satisfy these constraints, limiting the applicability. Using a scanning aperture object reconstruction can be performed from the diffraction data barring the need for additional support constraints of the object. The use of a scanning aperture however is inherently slow as it requires moving either the aperture or the object. Additionally an aperture makes poor use of available luminosity. This can be an obstacle for high harmonics sources where photon yield is precious. Work in this thesis focusses on the development of an alternative approach that promises a solution to both these problems. In this case, two coherent beams of light interfere to create a fringe pattern to illuminate the object, the technique is named interferometric illumination ptychography. No assumptions on the object are required as multiple images can be recorded by shifting the position of the interference fringes. A path delay of one optical cycle in one of the beams shift the fringes by a full period. Such a path delay can be achieved without mechanically moving parts. In this work a functional ptychographical setup with interferometric illumination is presented and explained. Specifically the author of this thesis has constructed the setup and developed several important parts of the reconstruction algorithm.

Four ingredients are required to achieve image reconstruction. Firstly a setup must be build. In the setup two fibres are used to create the pattern illuminating the object. The intensity of the diffraction pattern is then recorded by the camera. Secondly, diffraction of light propagating from the object to the camera must be understood. This allows for the development of a numerical tool to invert diffraction. Thirdly, the electric field of the illuminating electric field must be reconstructed, this illumination field is called the *probe*. Lastly an algorithm must be developed that can combine the intensity information of the diffraction patterns with the electric field information of the probe to reconstruct the amplitude and phase properties of the object.

In this thesis theory related to the necessary ingredients is treated, followed by an explanation of the methods and a demonstration of the results. The theory chapter will use diffraction theory to arrive at a mathematical expression called a *propagator* that can invert diffraction. The importance of coherent light and the theoretical resolution of the system will also be treated. An adaptation on the Gerchberg-Saxton algorithm to reconstruct the object is treated. Probe reconstruction from measured reference data and a priori knowledge is explained. A methods chapter will describe how the experiment was performed with special attention to demands that an interferometric illumination pattern places on the experiment. Some experimental tricks will be discussed as well. The results chapter will firstly discuss the performance of probe reconstruction and object reconstruction algorithms. Secondly the retrieved images are inspected. A resolution target

will be imaged to test the resolving power of this technique and a biological sample will be used to test phase imaging. Lastly an overview of achievements, problems and future possibilities is given.

# Chapter 2

# Theory

Image formation in a ptychographical setup is governed by the theory of diffraction. In some experiments [3, 16] diffraction patterns are captured in the Fraunhofer regime where the relation between an object and a measured diffraction pattern is straightforwardly given by a Fourier transform. In other experiments [17, 18] including this work diffraction patterns are captured in the Fresnel regime and extensive comprehension of diffraction theory is required to understand image formation. Insight into diffraction can be used to invert image formation and obtain a representation of the object. A serious problem is posed by the inability of detectors to measure phase directly. Phase information present in the object changes the intensity profile of the diffracted wave. Phase retrieval from diffraction data becomes an ill-posed inverse problem. Such a problem can be solved for using a phase retrieval algorithm if appropriate constraints are available. Initially [3] constraints are supplied by a single measurement of the Fourier transform of the image and the knowledge that the object is only present in a limited support area. Many objects are not localised in a small area, limiting the applicability of this technique. An alternative way to obtain necessary constraints is to measure multiple diffraction patterns. The diffraction patterns should be sufficiently different such that phase retrieval is possible. For ptychography this condition is fulfilled by varying the spatial distribution of the illumination. In this work interferometric illumination is used as it removes the need for mechanical movement and uses the full luminosity of the source, two important advantages over scanning aperture type ptychography. The illumination function is referred to as the probe. It must be known to enable image reconstruction and it can be considered as prior knowledge added to the reconstruction. However, the probe function is no longer a well defined scanning disc, instead it is an interference pattern susceptible to limited coherence lengths and variable fringe patterns. A scheme must be developed to accurately reconstruct the illumination function.

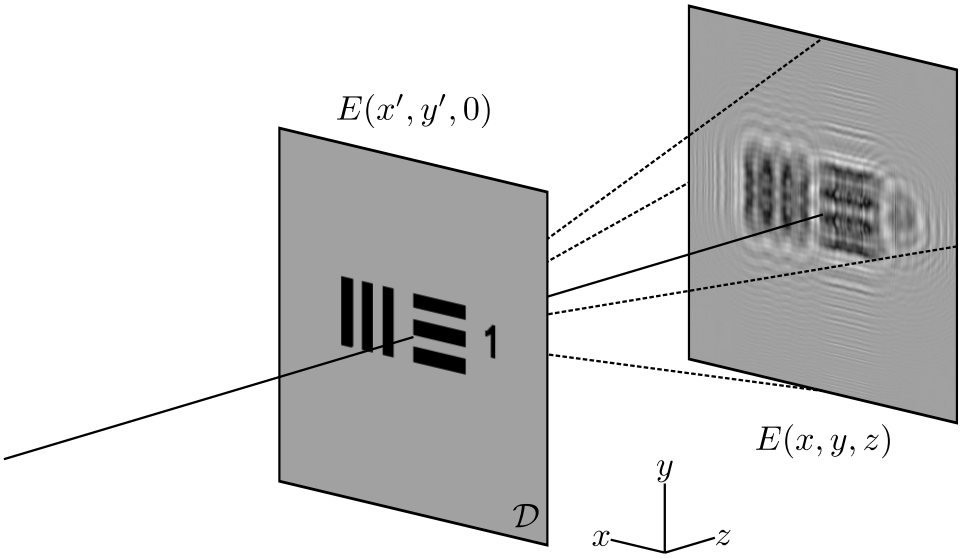


Figure 2.1: Geometry of propagating the electric field distribution between perpendicular planes. The diffraction pattern on the right is a result of light scattering on the left object.

## 2.1 Imaging theory and transfer functions

Each point in an electromagnetic disturbance can be considered as a point source. Propagation of an electromagnetic light field can be described by summing all waves originating from point sources. This is known as the *Huygens-Fresnel* principle.It is a specific case of the superposition principle in physics. Figure 2.1 shows two planes perpendicular to an optical axis oriented in the z direction. Suppose some object scatters light in a plane $z = 0$. The light field is referred to as the *exit wave* right after it scatters on the object. The distribution of the electric field at some other plane at distance $z$ can be calculated from considering all points in the exit wave as point emitters. This causes the object to blur and fringes to appear. Mathematically this process can be described as an integral over all point sources in the object plane with coordinate $\vec{r'} = (x', y', 0)$. The plane where the electric field is calculated has coordinate $\vec{r} = (x, y, z)$.

$$E(\vec{r}) = \frac{1}{\mathrm{i}\lambda} \iint_{\mathcal{D}} E(\vec{r'}) \frac{z}{|\vec{r} - \vec{r'}|} \frac{\exp(\mathrm{i}k|\vec{r} - \vec{r'}|)}{|\vec{r} - \vec{r'}|} \mathrm{d}x' \mathrm{d}y', \tag{2.1}$$

where E denotes the electric field in a plane perpendicular to the optical axis, k is the wavevector, $\lambda$ denotes the wavelength and $\mathcal{D}$ is the domain of integration. This result is for example derived in Goodman chapter 3 of Fourier Optics [19]. The $z/|\vec{r} - \vec{r'}|$ therm is caused from calculating the flux perpendicular to a surface. The dependancy on the inverse distance may be

understood from energy flow conservation through two concentric spheres. The surface of a sphere increases with $r^2$ and therefore the energy flow per unit surface must be scale with $r^{-2}$. Considering that the energy flow scales with the electric field squared and the electric field intensity scales with $r^{-1}$ this condition is indeed fulfilled.

The diffraction formula eq. (2.1) is an integral over a function in $\vec{r}'$ and a function that depends only on the difference of $\vec{r}$ and $\vec{r}'$, so it can be written as a convolution. This is a restatement of the Huygens-Fresnel principle and the superposition principle. It is possible to write

$$E(r) = E(r) * \frac{z}{\mathrm{i}\lambda|\vec{r}|}\frac{\exp(\mathrm{i}k|\vec{r}|)}{|\vec{r}|}. \tag{2.2}$$

The function on the right hand side of the convolution describes the blurring of a point and is therefore referred to as the *point spread function (PSF)*. The PSF may also describe the propagation from an object plane to a detector plane. In this sense it is used as an operator to propagate electric fields. It can be referred to as a *propagator*. As the PSF describes image formation, it is often used to characterize the resolving power of an optical instrument.

### 2.1.1 Fresnel and Fraunhofer diffraction

For sufficient large distances the spherical wavefront of a point source may be approximated as a parabola and intensity attenuation is dominated by the distance $z$ along the optical axis. This is the paraxial or small angle approximation. The PSF may be written as

$$PSF(r) = \frac{e^{\mathrm{i}kz}}{\mathrm{i}\lambda z}\exp\left\{\mathrm{i}k\frac{(x-x')^2+(y-y')^2}{2z}\right\}. \tag{2.3}$$

For z larger still the wavefront may be considered flat. Then the Fresnel diffraction equation 2.3 simplifies further to a Fourier transform of the object. This is called the Fraunhofer regime. A derivation of this property is straightforward from expansion of the therms of the integral, it is given in appendix A.4. The approximation is applicable if $z \gg k(x'^2 + y'^2)_{max}$. The distance $z$ is now so large that the source may be considered as a point. The Fraunhofer condition condition is often rewritten as

$$F = \frac{a^2}{z\lambda} \ll 1, \tag{2.4}$$

where a is the characteristic distance of the object. F is known as the *Fresnel number*. Figure 2.2 illustrates the diffraction pattern of objects for varying Fresnel numbers. The Fresnel number depends on the size of the structure. For identical propagation distances a small structure has already entered the Fraunhofer regime and is represented by its Fourier transform. A large structure on the contrary is still in the Fresnel regime. It resembles

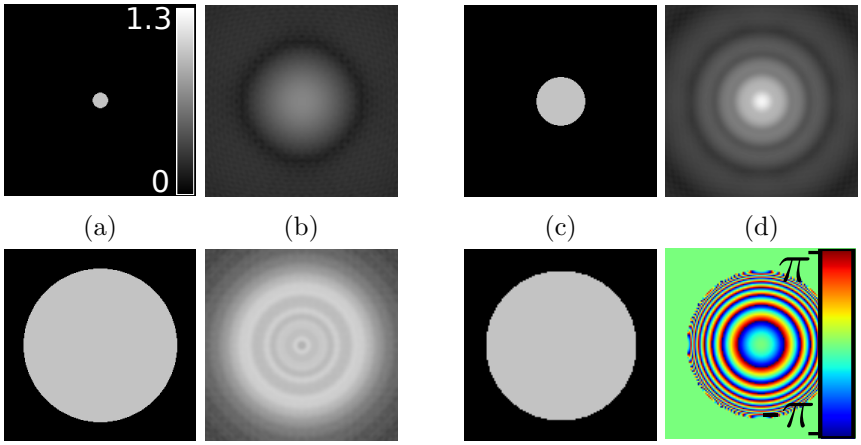


(a) (b) (c) (d)

(e) (f) (g) (h)

Figure 2.2: Objects (a,c,e) and diffraction patterns (b,d,f) for Fresnel numbers 0.1 (a,b), 1 (c-d) and 10 (e-f). Each pattern has been propagated over the same distance. The small object in (a) is in the Fraunhofer diffraction regime, indicating that the diffraction pattern is the Fourier transform of the object. The large structure (e) is in the Fresnel regime where the diffraction pattern still resembles the object. The intermediate structure (c) shows properties of both. The PSF is used to calculate the diffraction pattern from the object and vice versa, see section 2.1.3. The norm (g) and the phase (h) of the Fourier transform of the PSF is shown. The Colourbar in (a) is identical for (a-g), the cube root of the amplitude is displayed to increase readability. (h) has its own colourbar spanning $2\pi$.

its original shape. In the same figure the Fourier transform of the PSF is also shown. Refer to section 2.1.3 for more detail on the PSF.

### 2.1.2 Taking a shortcut trough Fourier space

The *convolution theorem* [20] states that Fourier transform of a convolution of two functions is equal to the product of the two fourier transformed functions:

$$\mathcal{F}\{f(x) * g(x)\} = \mathcal{F}\{f(x)\}\,\mathcal{F}\{g(x)\}. \tag{2.5}$$

Computationally a Fourier Transform of $n$ points costs $n \ln n$ operations to calculate [21], multiplication of two functions also costs n operations. Calculating a convolution by performing an integration costs $n^2$ operations. Obviously, computation time can be greatly reduced by Fourier transforming, multiplying and transforming back since $2n \ln n + n \ll n^2$ when $n \gg 1$. To make use of shorter computation time all convolutions are calculated through Fourier space.

### 2.1.3 Resolution of diffraction imaging in Fourier space

An upper limit to the resolution of an imaging system is set by the Helmholtz equation. Spatial frequencies higher than the inverse of the wavelength become evanescent and do not propagate into the far-field. This result can be derived starting from the Helmholtz equation applied to the Fourier transform of the electric field A at some position z.

The Helmholtz equation states

$$\nabla^2 E(x,y,z) + k^2 E(x,y,z) = 0, \tag{2.6}$$

at all source free points free points. This means

$$\frac{\mathrm{d}^2}{\mathrm{d}z^2} A(k_x,k_y,z) + (k^2 - k_x^2 - k_y^2) A(k_x,k_y,z) = 0, \tag{2.7}$$

where $k_z^2 = k^2 - k_x^2 - k_y^2$. The ordinary solution to this differential equation is

$$A(k_x,k_y,z) = A(k_x,k_y,0)\exp(\pm \mathrm{i} k_z z), \tag{2.8}$$

The sign of the exponent determines whether the wave will propagate forward or backward. The square root becomes imaginary for spatial frequencies larger than the wavevector. These spatial frequencies become evanescent field modes and cannot be measured in the far field. From Fourier transform of this result and application of the convolution theorem, the right-hand side function may be recognised as the Fourier transform of the PSF. This expression describes the transfer of spatial frequencies and is therefore named the *optical transfer function (OTF)*. In the far field, the OTF is described as

$$OTF(k_x,k_y,z) = \exp(\mathrm{i} k_z z) \qquad \text{for} \qquad k_x^2 + k_y^2 < k^2 \tag{2.9a}$$

$$OTF(k_x,k_y,z) = 0 \qquad\qquad\qquad\qquad otherwise. \tag{2.9b}$$

So propagation acts as a spatial frequency filter of the information present in the object. The OTF of free space propagation is a flat top disc with a spherical phase in the spatial frequency domain. The radius of the disc is determined by the norm of the wavevector. The norm depends both on the frequency of the light and refractive index of the material.

The resolution is further limited by the finite collection surface of the camera and finite extend of the source. Diffraction patterns spread out and may fall off the camera. Light falling of the camera contains information that can not be used for reconstruction. The limitation on the resolution as a result of the limited collection surface of the camera can be understood by considering the *angular spectrum*. Each spatial frequency in an image can

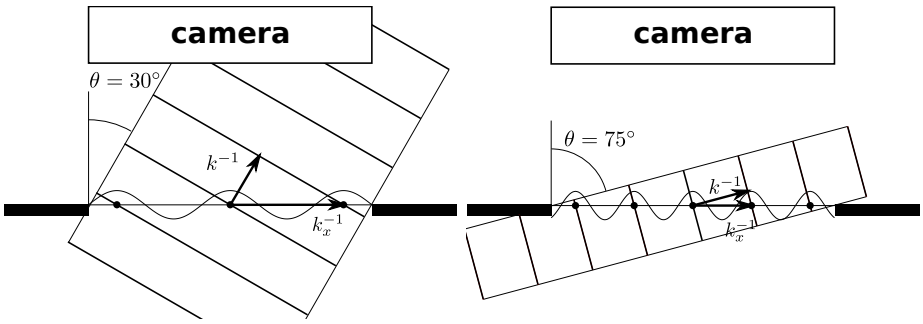


(a) (b)

Figure 2.3: Schematic showing the resolution limitations caused by the finite extend of the camera. Each spatial frequency in an image corresponds to a plane wave intersecting the image plane under an angle $\theta$. (a) the plane wave propagates and is captured by the camera. (b) the angle is too large to be captured by the camera.

be treated as the projection of an angled plane wave on the image plane. Figure 2.3 shows a plane wave crossing an image plane under an angle $\theta$. The projection of the plane wave on the image is a sinusoid whose period depends on the angle $\theta$ through

$$k_x = k \sin \theta, \tag{2.10}$$

where $k$ is the wavevector. In the angular spectrum each spatial frequency in the image corresponds to a plane wave propagation angle. For a finite source the resolution is now limited by the finite surface of the camera, since higher spatial frequencies fall off.

This picture may also provide additional insight into the properties of the OTF, equation 2.9. An image can be propagated by decomposing an image in its sinusoids, shifting all sinusoids according to their frequency and summing all sinusoids to reform the propagated image. The shift is created by the phase evolution in z expressed in $k_z z$. The angular spectrum links the spatial frequency in the image to the phase evolution in z.

Referring back to figure 2.3, the plane wave propagating under a 30° angle falls only partially on the camera. Therefore, only a part of the amplitude is transmitted to the object. The transfer of spatial frequency amplitude is now also a function of $\theta$. However, this process is not yet understood fully. As an approximation, the amplitude is considered to be transferred fully such that only the phase of spatial frequencies change during propagation. This treatment is similar to the transfer function of a lens with a *numerical aperture*.

## 2.2 From Object to Image

From the description of free space propagation in section 2.1, it is possible to proceed to a description of how the information available in an object is mapped to an image. Light originating from the two fibre tips form a fringe pattern that hits the object. This electric field distribution is called the *probe*, denoted $P$. The process of the probe being scattered by the object can be described by multiplication of the probe with an *object function* denoted $obj$. This object function characterises the object. The electric field distribution arriving at the detector is given by

$$E_{image}(x,y) = (obj(x,y)\ P(x,y)) * PSF(x,y), \tag{2.11}$$

where $PSF$ is the point spread function discussed in section 2.1 and $P$ is the probe function. In diffraction microscopy the multiplication of the object and probe is also often referred to as the *exit wave* [9]. This formula is simple enough and many microscopists attempt to make the PSF resemble a point, since this minimises the blurring properties of the imaging system. The blurring properties may also be described from inspection of the spatial frequency domain of the imaging process. Therefore it is interesting to look at the Fourier transform of equation 2.11

$$\mathcal{F}\{E_{image}\}(k_x,k_y) = \mathcal{F}\{obj\ P\}(k_x,k_y)\ OTF(k_x,k_y), \tag{2.12}$$

where the convolution becomes a product according to the convolution theorem. The OTF is the Fourier transform of the PSF. Equation 2.12 provides a useful framework to obtain additional insight in imaging. A bounded object is an object that is only non-zero in a finite domain. The bandwidth of a function is the domain where the function is non-zero. In Fourier theory any object which is bounded on one domain, has infinite bandwidth in the other domain. Since all object and probe functions are bounded in the Euclidean space, they have infinite bandwidth in Fourier space. The product of the probe and object then also has infinite bandwith. The exit wave still contains all information of the object provided the probe is known. The OTF is bandwidth limited, see subsection 2.1.3. Therefore propagation through free space is the bandwidth limiting step in the image formation. Any reconstruction of the object may only contain information already present in the diffraction patterns.

The diffraction pattern must be back propagated to reconstruct a phase image. From equation 2.11 back propagation can be achieved by a convolution with the inverse of the PSF. So, backproagation is performed by inverse filtering the diffraction pattern with the PSF. The PSF is determined purely by free space propagation over a distance $z$. From the discussion in section 2.1.3 the OTF may be considered a flat-top disc as in eq. (2.9). The radius of the flat-top disc is limited by the numerical aperture $k_{max} = 2\pi\, n\, \sin(\alpha)/\lambda$

with $n$ the refractive index, $\alpha$ the maximum angle which is still captured by the imaging system and $\lambda$ the wavelength of light used. The phase of the OTF is a spheroid centred at $k = 0$ with a radius of curvature equal to $k$. The spheroid radius increases as the propagation distance $z$ increases. As a result of its flat-top amplitude profile, the OTF may be inverted by taking its complex conjugate.

Noise amplification [22, 23]is a serious problem when performing inverse filtering. If the transfer efficiency of a spatial frequency is very low, the signal of that spatial frequency in the image is likely dominated by noise. Application of inverse filtering enhances the noise as well as the signal. Due to the flat-top amplitude profile of the OTF, noise amplification as a result of inverse filtering is not expected to be a big problem. It is prudent however to be aware of the possibility of noise amplification.

**Inverse filtering or back propagating is possible due to the flat-top amplitude of the transfer function. This works only for coherent imaging.**

### 2.2.1 Coherent image formation

Ptychography relies on interference of light to resolve phase information. Interference is caused by a fixed phase relation of two light sources [24]. If contributions from two light sources have a fixed phase relation, the sources are said to be *coherent*. If the phase relation of two sources is varying wildly, the light is said to be incoherent and no phase information can be resolved. The influence of the phase on the camera intensity can be derived by considering interference from two point sources.

Suppose two sources emitting light that interfere in some point [24]. The electric field at that point is the sum of the two complex source contributions. The phase between the two sources determines whether there is constructive or destructive interference. A camera measures the intensity of the light averaged over a time much longer than an optical cycle. For the two source model the intensity is determined by

$$I_{camera} = \lim_{T\to\infty} \frac{1}{T} \int_0^T \left| A_1 e^{\mathrm{i}\phi_1} + A_2 e^{\mathrm{i}\phi_2 + \phi'(t)} \right|^2 \mathrm{d}t, \tag{2.13}$$

where $A_{1,2}$ denotes the amplitude of the two point sources and $\phi_{1,2}$ the phase of the two point sources. The $\phi'(t)$ variable denotes how the phase between the two points sources varies over time. $\phi'(t)$ will determine whether the imaging is coherent or incoherent. For a coherent source [25] the phase relation is fixed. Since the intensity is insensitive to the absolute phase, $\phi'(t)$ is chosen 0. Expression eq. (2.13) is considered for a coherent source:

$$I_{camera} = A_1^2 + A_2^2 + 2A_1A_2\cos(\phi_1 - \phi_2). \tag{2.14}$$

The time average defaults to unity since there is no more time dependence in the expression. The expression shows that the intensity depends

on the phase of the two sources, so there is interference.
For *incoherent sources* the phase relation varies a lot, such that the phase of the two points is random. The average over time becomes an average over the $\phi'$.

$$\begin{aligned} I_{camera} &= \frac{1}{2\pi}\int_0^{2\pi} A_1^2 + A_2^2 + 2A_1A_2\cos(\phi_1 - \phi_2 - \phi')\mathrm{d}\phi' \\ &= A_1^2 + A_2^2. \end{aligned} \tag{2.15}$$

The intensity at the camera is independent of the phase of the two sources and therefore incoherent light cannot be used for phase imaging.

The argument above for two points may be expanded to any number of points. Coherent imaging can be considered as interference of many coherent sources. It is now possible to use the above insight to obtain a general expression for coherent imaging system without having to do a more formal derivation. The expression for the image on a camera becomes

$$I_{coherent}(x,y) = \left|\left[obj(x,y)\ P(x,y)\right] * PSF(x,y)\right|^2. \tag{2.16}$$

The intensity on the camera depends on the phase of the object and the bandwidth of the system is determined by the $PSF(x,y)$.

## 2.3 Inverse problems and reconstruction algorithms

### 2.3.1 Introduction to ill-posedness of inverse problems

Phase retrieval in ptychography is an example of an ill-posed inverse problem. For this type of problem an extended theoretical framework exists to help solve them [26]. Inverse problems appear in pairs. If the solution to one problem is known, the solution to the other problem can be calculated. In case of ptychography, the inverse problems are electric fields in different planes. If the electric field distribution is known in one plane, electric field distributions in all other planes can be determined from eq. (2.3). Usually there is some hierarchy in the set of problems determined by cause and results or the loss of information when transforming from cause to effect. For ptychography the cause is the object that scatters light and the result is the diffraction pattern that hits the camera. To calculate the diffraction pattern from the object is called the direct problem and to calculate the object from the diffraction pattern is called the *inverse problem*. Since the transfer function is bandlimited, see section 2.1.3, the object contains more information than the diffraction pattern. Specifically, all objects that are the same in the in-bandwidth domain, but different out of the bandwidth domain, cause the same diffraction pattern. The problem is ill-posed as

multiple objects may cause identical diffraction patterns. The search for a solution to an inverse problem is further hampered by noise. The object no longer causes a unique diffraction pattern in the presence of noise. Instead, there is a probability that an object will create a measured diffraction pattern. Ill-posedness can be countered by adding additional knowledge about the object, this type of knowledge is called *a priori* or prior knowledge. For example the object can be assumed to have a certain smoothness. Phase retrieval is by itself an inverse problem as information is lost when the detector measures the intensity of the incoming wave. Ptychography aims to cure ill-posedness by measuring multiple different diffraction patterns. An algorithm is then used to find the object which is most likely to satisfy this set of constraints. However ambiguity may still remain due to noise and the systematic absence of information in the measured diffraction patterns. Section 2.2.1 discusses how phase information of the object is measured on the camera. The next section will discuss an adaption on the Gerchberg algorithm aimed at retrieving the phase information of the object.

### 2.3.2 Nonlinear retrieval through an adapted Gerchberg algorithm

Image formation is non-linear since the camera measures the intensity which is the absolute square of the electric field, thereby losing phase information of the incoming electric field, see section 2.2.1. Often non-linear problems are linearised to make use of the framework of linear algebra.[1] The norm of the electric field is known from the intensity however and Gerchberg developed an algorithm [27] that can incorporate constraints from multiple domains to find a solution. This technique has been further developed by Fienup [5, 6]. For ptychographical retrieval the Extended Ptychographical Iterative Engine (EPIE) from Rodenburg [8, 9] has been developed to find the object which satisfies electric field amplitude constraints from various measurements. The algorithm imposes constraints of diffraction measurements by solving the direct problem of what diffraction pattern is expected based on the object guess. The object guess is improved by replacing the amplitude of the diffraction guess with the measured amplitude. If the object guess is correct the diffraction guess will match the measured diffraction pattern. Furthermore already in 1972 [4] it was shown that the original al-

[1] An example of a non-linear solution method is the inversion of the intensity square by undoing the autocorrelation in Fourier space. Suppose an electric field $(\mathrm{E})$ with frequency domain $\mathcal{K}$ is squared, from the convolution theorem, the Fourier transform of the intensity is the autocorrelation of the Fourier transform of $E$ and has domain $2\mathcal{K}$. The autocorrelation maintains the number of degrees of freedom as the domain of the autocorrelation is twice as big, but also Hermitian. Since both the electric field and the intensity have the same number of degrees of freedom, a single intensity image can be used to reconstruct a sharp phase image! Sheppard [7] proposes a method to directly invert the autocorrelation in case of cylindrical symmetry. If Kobus reads this, he earns a chocolate egg.

gorithm reduces the root mean square error each iteration. The quadratic error is defined as the difference between subsequent iterations squared. The algorithm used for this work is largely based on the work of Rodenburg et al. Figure 2.4 depicts schematically the steps in the algorithm. For simplicity the $x$ and $y$ index have been dropped, all elements are understood to be two-dimensional arrays.

1. Start with a guess of the solution $f_0$ in the object domain $\mathcal{O}$, the default guess is $f_0^{\mathcal{O}} = 0$.

2. Transform the solution to the domain of measurement $j$ called $\mathcal{M}_j$ using the appropriate propagator.

3. Impose the constraint of the measurement on the solution. For this type of Gerchberg algorithm the amplitude of the solution at $\mathcal{M}_j$ is known, so the amplitude of the solution guess is replaced by the measurement amplitude.

$$\tilde{f}_i^{\mathcal{M}_j} = |g^{\mathcal{M}_j}| \arg(f_i^{\mathcal{M}_j}). \tag{2.17}$$

   The constrained object guess is denoted with a tilde ($\tilde{}$). The operation to replace the amplitude is nonlinear.

4. Propagate the solution guess back to the object domain $\mathcal{O}$.

5. Obtain a new guess $i+1$ for the solution in the object domain using an update function of the form

$$f_{i+1}^{\mathcal{O}} = f_i^{\mathcal{O}} + U\big(f_i^{\mathcal{O}}, \tilde{f}_i^{\mathcal{O}}\big), \tag{2.18}$$

   $U$ being the update function. It will often include a feedback parameter and may be nonlinear.

The object guess may be represented in the object domain $\mathcal{O}$ or the measurement domain $\mathcal{M}_|$ without loss of information. Diffraction patterns should be sufficiently different in order to reduce ambiguity in possible objects, i.e. reduce ill-posedness. The algorithm attempts to find the object which is most likely to satisfy all diffraction constraints, therewith limiting the ill-posedness.

### 2.3.3 Structured illumination Ptychography retrieval

The illumination function for interferometric illumination ptychography is created by overlapping two coherent beams under an angle to create a fringe pattern of alternating constructive and destructive interference. The two beams act as an interferometer see section A.2. By changing the pathlength of one arm slightly the fringes shift and the illumination pattern is changed.

The retrieval scheme used for reconstruction implements the algorithm described in section 2.3.2.

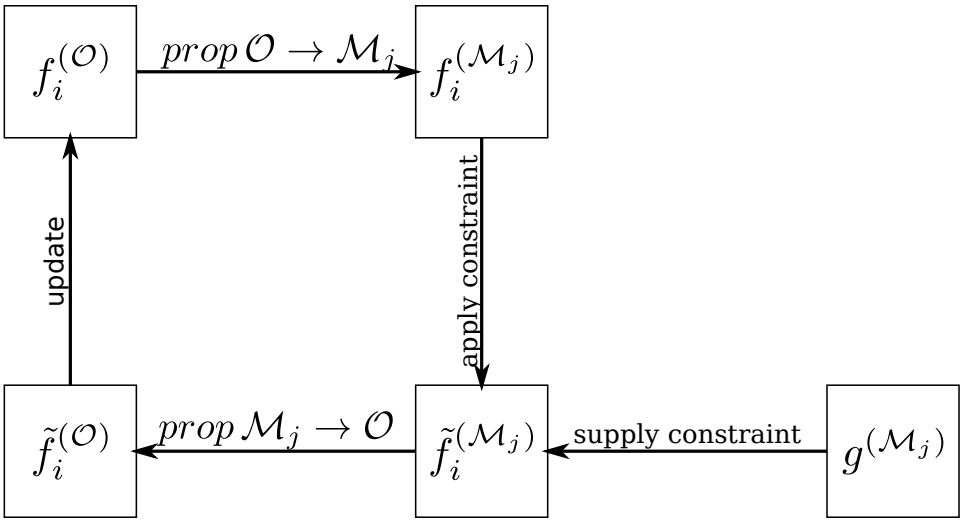


Figure 2.4: The adjusted Gerchberg reconstruction algorithm as described in [14, 16]. For a detailed explanation and declaration of symbols refer to section section 2.3.2.

1. Make a first guess of the object $f_0^{\mathcal{O}}$

2. To propagate to the measurement domain $\mathcal{M}_j$ multiply the object guess with the probe function $P_j$ to obtain the exit wave. Then propagate the exit wave over a distance z.

$$f_i^{\mathcal{M}_j} = \big(f_i^{\mathcal{O}} P_j\big) * PSF(z). \tag{2.19}$$

   The $PSF$ is the same for all measurements as the propagation distance $z$ and the wavelength are identical for each diffraction pattern.

3. The amplitude of the solution guess in the diffraction domain is replaced by the measured data constraint.

$$\tilde{f}_i^{\mathcal{M}_j} = |g^{\mathcal{M}_j}| \arg(f_i^{\mathcal{M}_j}). \tag{2.20}$$

4. The inverse propagator is applied to the constrained diffraction guess to obtain $\hat{f}_i^{\mathcal{O}}$

$$\tilde{f}_i^{\mathcal{O}} = P_j^{-1}\big(\tilde{f}_i^{\mathcal{M}_j} * PSF^{-1}(z)\big). \tag{2.21}$$

   A division is made by the probe function to obtain the solution guess in the object domain. Zero-values in the probe cause numerical divide-by-zero problems. These problems can be circumvented by replacing zero values with a very low value.

5. The solution guess is updated using the previous iterations and the update function. For research done in this thesis the update function from equation eq. (2.18) takes the form

$$U\big(f_i^{\mathcal{O}}, \tilde{f}_i^{\mathcal{O}}\big) = \epsilon \frac{|P_j|^2}{\max(P_j)^2}\big(\tilde{f}_i^{\mathcal{O}} - f_i^{\mathcal{O}}\big). \tag{2.22}$$

The update function has a large value for strongly illuminated points. Therefore these points have a big contributions to the correction on the image. This partly solves the problem of dividing by a zero probe function. It is interesting to investigate the update function further as it is an important part of the reconstruction algorithm. The focus of this thesis is elsewhere however.

## 2.4 Probe reconstruction

The probe function is the electric field distribution that hits the object. For interferometric illumination two fibres are used as an interferometer to create a fringed illumination pattern. The fully characterised probe function must be available as prior knowledge in order to reconstruct images. However cameras are only sensitive to the intensity of the electric field. It is possible to reconstruct the electric field with knowledge of the setup and a reference intensity measurement. To do this it is necessary to understand how the probe function is formed.

Light exits single-mode fibres with a 0.12 NA spatial bandwith limited Gaussian distribution. Therefore the electric field distribution may be described as a Gaussian beam in the paraxial regime with the focus at the end of the fibre, [2] see chapter 6 of Hooker and Webb [28]. The electric field distribution at distance $z$ from the fibre tip may be written as

$$E(r,z) = A\exp\Big\{-\Big[\frac{r}{w(z)}\Big]^2 + \frac{\mathrm{i}kr^2}{2R(z)}\Big\} \tag{2.23}$$

Where A is a constant containing any phase and amplitude offset. The precise value of A is not of interest as the amplitude offset of the electric field can be directly controlled using the luminosity of the source and the intensity is insensitive to any phase offset. The amplitude and phase distributions are much harder to determine from the experiment and therefore it is useful to consider these theoretically. The system has radial symmetry so $r$ and $z$ represent the radius and height coordinates in the cylindrical system. $w(z)$ is the width of the beam at distance $z$, $R(z)$ is the radius of curvature of the

[2] The paraxial approximation is extremely good for this setup, for a 0.12 NA fibre the relative propagation distance error is only $8.4e^{-6}$.

wavefront. These beam characteristics may be approximated if the beam is far from the focus

$$w(z) = w(z_0)\sqrt{1 + \Big(\frac{z - z_0}{z_R}\Big)^2} \qquad \approx w(z_0)\frac{z - z_0}{z_R}, \tag{2.24a}$$

$$R(z) = z - z_0 + \frac{z_r^2}{z - z_0} \qquad \approx z - z_0, \tag{2.24b}$$

$$z_R = \frac{\pi w(z_0)^2}{\lambda}, \tag{2.24c}$$

where $z_0$ is the z position of the focus. $z_R$ is the Rayleigh range, it may be estimated as $60\mu m$ for a SM fibre, which allows for $z - z_0 \gg z_R$. The beam used in the ptychography experiment has three variables: Firstly the position in $r$ of the focus, this can be adjusted by translating $r \to r - r'$. Secondly the z position, which can be tuned by choosing the appropriate $z_0$. Thirdly the angle of the beam, as discussed in section 2.1.3, the angle may be adjusted by multiplying with $\exp(\mathrm{i}k_\theta r)$ where $k_\theta$ is the angular frequency corresponding to the direction of propagation. The electric fields from each fibre may be written as

$$E_1(r, z) = A_1 \exp\Big\{\Big(\frac{r - r_1}{w(z_1)}\Big)^2 + \frac{\mathrm{i}k(r - r_1)^2}{2z_1} + \mathrm{i}k_{\theta,1}\Big\} = |E_1|e^{\mathrm{i}f(r)} \tag{2.25}$$

$$\begin{aligned} E_2(r, z) &= |E_2|e^{\mathrm{i}f(r)} \exp\Big\{\mathrm{i}(k_{\theta,2} - k_{\theta,1})r + \frac{\mathrm{i}k(r - r_2)^2}{2z_2} - \frac{\mathrm{i}k(r - r_1)^2}{2z_1}\Big\} \\ &= |E_2|e^{\mathrm{i}f(r))}e^{\mathrm{i}g(r)}, \end{aligned} \tag{2.26}$$

where $f(r)$ and $g(r)$ are parabolic functions with coefficients that can directly be deduced from above formulas. The function $f(r)$ drops out when the intensity pattern is calculated:

$$|E_1(r) + E_2(r)|^2 = |E_1|^2 + |E_2|^2 + 2|E_1E_2|\cos g(r). \tag{2.27}$$

The norm of E-fields $|E_{1,2}|$ can be obtained directly from measuring each branch of the interferometer separately. The electric field of the probe can be reconstructed if $g(r)$ is known. g(r) may now be referred to as the phase function. It can be obtained from the Fourier transform of a reference probe intensity measurement. Figure 2.5b shows the Fourier transform of the probe. Three peaks are visible, the outer two peaks relate to the fringes and the inner peak relates to the intensity distribution from equation 2.27. In the paraxial approximation $g(r)$ may be written as $ar^2 + \vec{b} \cdot \vec{r} + c$. The electric field can be reconstructed if these parameters are obtained.

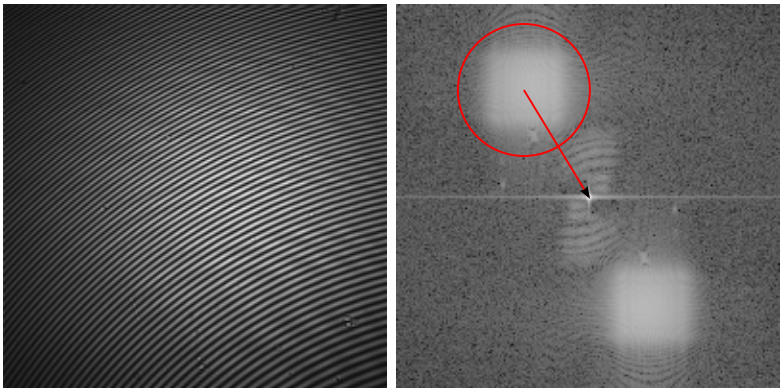

(a) curved probe (b) Fourier transform

Figure 2.5: (a) A probe with strongly curved fringes, visible in (b) as extended peaks around a main fringe frequency. The red circle in (b) is used as a mask to determine the central frequency and extract the fringe curvature, see 2.4.1.

### 2.4.1 Probe reconstruction in case of large experimental drift

In some cases, the probe function changes significantly in the time between a probe reference measurement and recording diffraction measurements. In these cases it is advantageous to make a separate reconstruction of the offset, linear and quadratic order terms. Probe reconstruction can be succesful for drifting probe function if the quadratic term remains constant. The linear and offset term can then be adjusted for each diffraction pattern separately. The linear phase term in $g(r)$ determines the central fringe frequency, it is obtained by taking the weighted average of the area inside the red circle in figure 2.5b. The quadratic therm and higher order aberration in $g(r)$ cause the outer peaks to spread out. To obtain the quadratic phase first the red-circled area is selected using a mask. This way, from expression 2.27 $|E_1E_2|\exp(\mathrm{i}g(r))$ is selected. Subsequently the masked area is placed in the middle of the image according to the red arrow in the figure. In real space this corresponds with a multiplication of $\exp(-\mathrm{i}\vec{b}\vec{r})$, such that $|E_1E_2|\exp(\mathrm{i}(ar^2+c)$ is left. The phase is taken from this the expression. Now the value for $a$ is known. Finally the phase offset $c$ is easily obtained from taking the phase of the central frequency.

A drawback of this approach is the limited possibility to reconstruct curved probe functions, i.e. a large quadratic parameter. Possibly, this may be explained as follows. As curvature increases, the outer peaks spread outside of the masked area. Quadratic and higher order therms are no longer well accounted for and reconstruction fails. Another possibility is that also the quadratic coefficient drifts for strongly curved fringes. In effect this probe reconstruction method demands that fringes are very straight.

### 2.4.2 Probe reconstruction for curved fringes

Generally, interference fringes are curved. Fringes are straight only in the special case that both interferometer arms have the same curvature, caused by an equal propagation distance through free space. A second reconstruction method to reconstruct curved fringes has been developed by the author of this thesis. This technique makes direct use of the properties derived in eqs. (2.25) to (2.27). This method works rather straight forward by extracting the function $g(r)$ directly.

Again, from a reference measurement, $|E_1|$ and $|E_2|$ are known. By subtracting and dividing these fields from a probe reference measurement $\cos g(r)$ is obtained:

$$\cos g(r) = \frac{|E_1(r) + E_2(r)|^2 - |E_1|^2 - |E_2|^2}{2|E_1 E_2|}. \tag{2.28}$$

It is important to subtract any background offset due to e.g. a camera dark current as errors will propagate into the reconstruction result. Figure 2.6 shows a detail of $\cos g(r)$. Subsequently the phase function $g(r)$ is obtained by masking out the bottom half of the Fourier transform. Due to the Hermitian property of the Fourier transform of a real function, no information is lost during this step. A cosine can be written as a sum of two complex exponents. The mask in Fourier domain selects a single complex exponent. Now $g(r)$ modulus $2\pi$ can be obtained directly from the phase of the real space image:

$$g(r) \mod 2\pi = \text{angle}\big(e^{ig(r)}\big). \tag{2.29}$$

Any change in the phase offset c is obtaining from the phase of the central frequency as before. The change in c is then added to $g(r)$ to account for fringe drift. This probe reconstruction is well able to reconstruct curved fringes robustly in a stable environment. Any drift in the fringe frequency should be smaller than one oscillation within the field of view.

Now $|E_1|$, $|E_2|$ and $g(r)$ are known and the electric field can be reconstructed directly from eqs. (2.25) and (2.26)

### 2.4.3 Errors induced by insensitivity to parabolic phase offset

It is impossible to reconstruct the residual phase function $f(r)$ from intensity measurements as the intensity is insensitive to them. Still. It is worthwhile to consider the effect of this function. Again from the paraxial approximation $f(r)$ is a parabola. The parameters of the parabola $a'$, $b'$ and $c'$ can be accounted for as follows. A total phase offset is irrelevant so $c'$ is ignored. A linear phase term relates to a change in propagation direction, the object will be reconstructed in a different position if such a phase shift

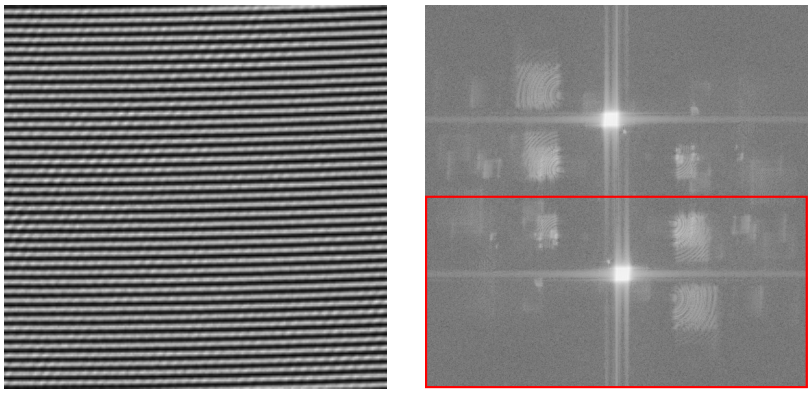

(a) Detail of $\cos g(r)$. (b) Fourier transform of $\cos g(r)$.

Figure 2.6: Probe reconstruction for curved fringes. $\cos g(r)$ is obtained from subtraction and division of reference electric fields $E_{1,2}$. The red boxed area in the Fourier transform is replaced by zeros to obtain a single complex exponent of the cosine. Subsequently $g(r)$ is obtained from the phase of the real space image.

is applied to both branches. A position shift is mostly not of interest for the interpretation of the image. So $b'$ is irrelevant due to *propagation direction invariance*. A residual parabolic wavefront $c'$ creates a divergent beam. As a result of the divergence, the diffraction pattern is enlarged as it propagates, creating lensless magnification. Lensless magnification may be desirable as camera pixel sizes are often much larger than the resolution present in the diffraction signal.

# Chapter 3

# Methods

## 3.1 Introduction

A scanning disc Fourier transfrom ptychography setup [16] can be rather straightforward. In principle the setup needs only a light source, an aperture, the object and the collection camera. The probe function is a well defined disk that is scanned over the object and there is no precise alignment required. Interferometric illumination ptychography offers several advantages over scanning-disc aperture ptychography as mentioned in the introduction, but also brings several complications.

An interferometric illumination is created by interference of two sources. So, like an interferometer the setup must have two arms. The interferometric signal is sensitive to vibrations, so the setup must be stable. The setup is chosen to be fibre based due to the flexibility that fibre optics offer. Any type of phase imaging must be performed with coherent light, see section 2.2.1. The path length difference may be referred to as the path delay. It must be smaller than a tolerance provided by the coherence length of the laser, see section A.2. The coherence length can be estimated to be $200\mu m$ for a 450nm, 1nm bandwidth laser, see equation A.5. The setup should be aligned within this tolerance.

In case of probe reconstruction for straight fringes, free space propagation distance should be identical for the two fibres, see section 2.4. The tolerance for the difference in free space propagation distance is experimentally determined to be 0.1 mm. Finally as discussed in section 2.1.3 the sample should be placed close to the camera to maximise the numerical aperture.

A diverging illumination beam is advantageous as it projects a magnified version of the diffraction pattern on the camera [15], the magnification is increased if the object is placed closer to the fibre tips or the camera is placed further away. Whenever possible a higher magnification is desirable.

In this chapter first the setup, built by the author of this thesis, will

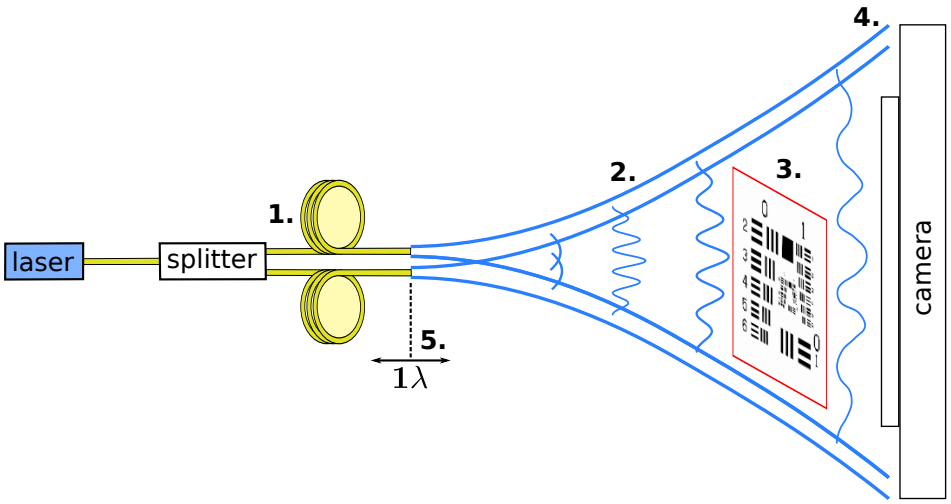


Figure 3.1: Schematic of a interferometric illumination ptychography setup. See section 3.2 for detailed information.

be described. Attention will be spend to explain how the setup satisfies various demands mentioned above. Finally, a data collection procedure will be treated in order to aid reproducibility.

## 3.2 Setup

To make sure the imaging is coherent, the interferometer branches must have equal lengths within the tolerance of the coherence length. A branch length is determined by the sum of the fibre length from the splitter and the free space propagation distance. The exact coherence length depends on the spectrum of the laser and therefore on the current and temperature of the laser. However from early experiments it is clear that the coherence length is smaller than 0.5 mm. Furthermore the coherence length is an oscillating function, see appendix A.2. For imaging only the top of the function at zero path delay where the coherence is unity and constant can be used. The path delay must less than 0.1 mm to be sufficiently close to zero displacement. Additionally for sufficient fringe contrast the branches must also have equal intensity. Figure 3.1 shows a schematic overview of the setup. 1. A simple fibre-coupled diode laser is used as a light source. Blue light is guided through a fibre unto a fibre beam splitter. Single-mode fibres are used to ensure spatial coherence. The fibres have a bare fibre ending from which a divergent beam is created. 2. The beams overlap and interfere to create a fringe pattern. This fringe pattern is called the *probe*. 3. The probe is scattered by the object to form the *exit wave*. The scattered light propagates through free space. 4. At the camera plane a diffracted version of

the scattered light is recorded by the camera. 5. Several images are needed to reconstruct an object. A full period shift of the probe fringes is achieved by changing an interferometer arm length by a single wavelength. The single wavelength shift requires no moving parts in the setup. Thermal induced variations in the path delay shift fringes sufficiently to create diffraction patterns for reconstruction.

In summary, the setup must satisfy the following requirement: Firstly beams from the fibre tips must overlap on the camera. Secondly the fibre tips must be close together in order to create the desired fringe frequency. Thirdly The setup must have equal arm path length for coherence. Lastly the distance from the fibre tip to the camera must be equal for probe reconstruction. Figure 3.2 shows a picture of the setup. It contains the following components:

1. 2x2 light mixer. One arm remains unused so it acts as a 1 to 2 fibre splitter. For experiments two splitters where used: Thorlabs FC632-50B-FC with a splitting ratio >20:1 used off spec and Thorlabs FC488-50B-FC with a splitting ratio of 3.4:1 slightly off spec.

2. Thorlabs ADAFC2 FC/PC to FC/PC mating sleeve. These mating sleeves can be used to create straight fringes by pulling the fibre head slightly out of the sleeve. This induces losses that need to be compensated for.

3. SM fibre for 400-680nm with 0.12 NA, Thorlabs serial number SM-405XP. The end is bare fibre, cleaved manually using Thorlabs XL411.

4. Fixed arm mount, placed directly on the opticle table. Figure 3.3 shows the home made mount. The mounts allow for control over the $\phi$, $\theta$ and y direction, see section 3.2.1.

5. Moving arm mount, it is mounted on two translation stages. Additional to the three degrees of freedom offered by the mount, the translation stages also offer $x$ and $z$ translation.

6. Linear polariser in a rotating mount. The polariser guarantees that light from both arms are in the same polarisation state. Additionally it provides an attenuation mechanism.

7. Sample, pressed close to the camera to maximise NA for maximal resolution.

8. Camera, IDS UI-5482LE-M CMOS mono chip board camera with 2.2 $\mu m$ square pixels. The camera can be controlled and scripted using python.

9. pigtailed 450 nm diode laser (shown schematically), Thorlabs serial number LP450-SF15.

10. laser driver (shown schematically), operated in constant current mode, Thorlabs serial number LPC-202C. For later experiments a new laser driver with additional diode temperature control was used, Thorlabs serial number CLD1011LP.

11. Digital delay generator 'stanford box' (shown schematically) serial number DG645.

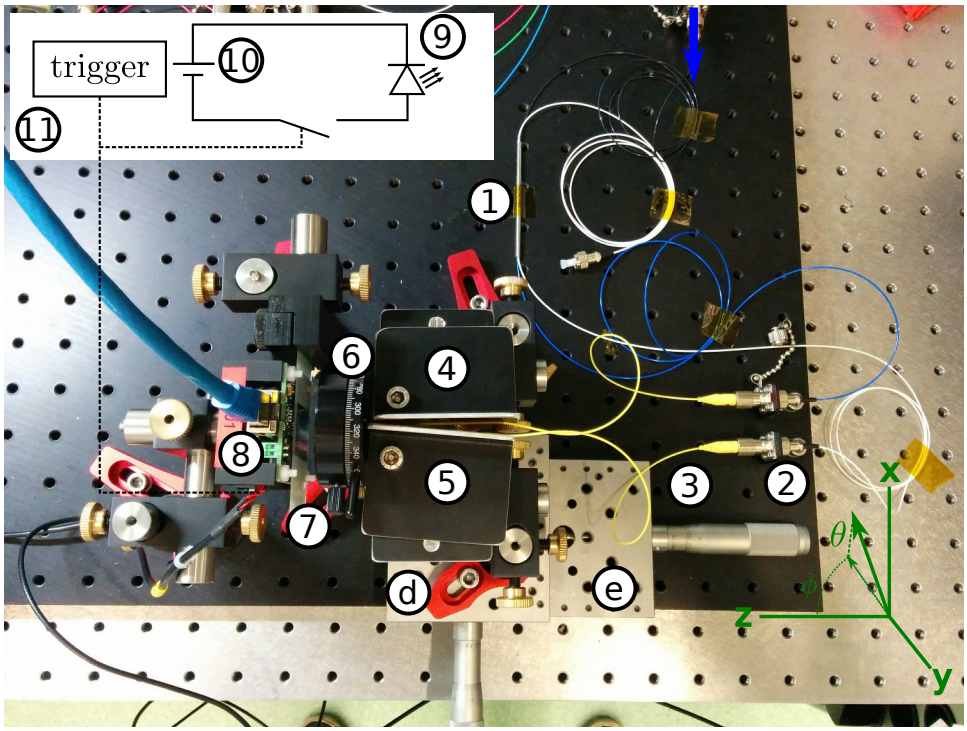


1. fibre splitter
2. fibre mating sleeve
3. $400 - 480$ nm SM fibre
4. fixed arm mount, 3 DOF
5. moving arm mount, 5 DOF
6. rotating polariser
7. sample
8. camera
9. fibre coupled diode laser
10. laser driver
11. stanford box trigger

Figure 3.2: picture of the setup. DOF stand for degree of freedom. The blue arrow indicates where light enters the setup.

### 3.2.1 Interferometer arm mounts

Fringes must be spaced close enough to ensure sufficiently different probe function, but far enough to avoid aliassing, see section section A.3. As a rule of thumb a fringe period should be 4 pixels, half the nyquist frequency. The fringe frequency is determined by the distance between the fibre tips. The displacement in z is not of influence. It is possible to estimate the tip displacement $\Delta x$

$$\frac{d}{\lambda} = \frac{l}{\Delta x}, \tag{3.1}$$

where l is the free space propagation distance and $d$ is the fringe period. This holds true if $l$ is much larger than $d$. From this the fibre tip displacement can be estimated $\Delta x = l\,\lambda/d$. For $l$ is 5 mm and the fringe frequency is 4 pixels of $2\mu m$ size each, this gives an estimate for the tip displacement of 0.5 mm. The plastic coating of the fibres is too thick to allow the fibre ends to be placed 0.5 mm apart, therefore bare fibres must be used. The fibre mounts should allow the fibres to be placed close together, while offering good control over the angle of the fibre. The mount consists of two plates. The bottom plate is screwed to a lens-mount with two fine adjustment screws denoted b and c, allowing for translation in the $\theta$ and $y$ direction. The top plate can rotate over the bottom plate around a single screw denoted a in order to allows for $\phi$ translation. The fibre is taped to the mount with kapton tape over a length of 5 cm for pull relief and the bare fibre extends less than 5 mm to avoid vibration of the fibre tip. The mounts have been co-designed and build by Nik Noest.

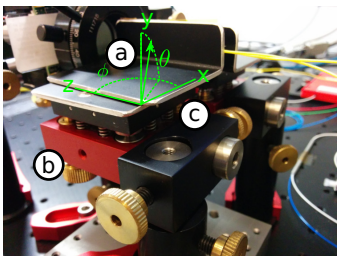


ⓐ $\phi$ control ⓓ x control
ⓑ $\theta$ control ⓔ z control
ⓒ y control

Figure 3.3: Mount for 5 degrees of freedom for fibre tip position and direction control. (a-c) shown in this image. (d,e) translation stages shown in figure 3.2.

### 3.2.2 Alignment for straight fringes and maximal fringe contrast

Initially, only the reconstruction technique fro straight fringes was available. Fringes are straight if the free space propagation distance is equal. As an additional demand, the path length of the arms should be equal within the coherence length in order to do coherent imaging. An experimental difficulty is created as the bare fibre ends can be cut to length with a precision of roughly 1 mm. Probe reconstruction for straight fringes can be successful up to a free space length difference of 0.1mm. The laser has multiple modes and therefore the coherence shows a sinusoidal signal, see section A.2. The tolerance of equal length arms is experimentally determined to be 0.1 mm. Over this length, the coherence is stable and close to unity, see appendix A.2. To compensate unequal fibre lengths an alignment procedure has been created. The procedure aims to create a zero path delay and equal free space propagation length. As a consequence, the setup is destabilised, which has detrimental effects on the repeatability of the experiment.

The path delay can be adjusted by pulling the fibre end out of the FC/PC to FC/PC mating sleeve. Consequently, firstly the connection is destabilised.

Secondly the intensity in that specific arm is attenuated by several orders of magnitude. To compensate for the attenuation, the combination of a linear polariser and stress induced birefringence, see section A.1 is used to attenuate the other arm as well. This is experimentally challenging since the attenuation from the connector sleeve is easily 20dB. To compensate, the other arm must be sent almost perpendicular polarised through the polarizer. This destabilises the setup, as slight variations in stress may induce large variation in arm intensity. In this case it can be helpful to have an unequal fibre splitter 1, denoted in figure 3.2. The shorter arm can be attached to the brighter splitter output to counter attenuation. It is not viable to induce losses by bending, since for 452nm light the bending radius is similar to the breaking radius of the fibre.

The alignment procedure looks as follows:

1. Use the Fourier image to find the point where fringes are straight, by moving in z using the translation stage.
2. Find the arm length difference by translating z up to the zero path length difference point. This length can be used as a guide for steps 3 and 4. For a laser lasing at multiple modes it can be hard to find this point since the fringe modulation as a function of z oscillates. In this case, it is useful to lower the laser current below the diode threshold so that the diode acts as a lamp with a short coherence length and the point of zero path delay can be found easily. It may be necessary to increase collection times of the camera to compensate for the lower laser brightness.
3. Pull the fibre end out of the sleeve slightly.
4. adjust the beam intensity to be equal using stress induced birefringence and a polariser.
5. Repeat steps 3 and 4 until you are at zero path length difference. Use the fringe modulation to judge this point.

### 3.2.3 Setup drift

The setup suffers from thermal and mechanical drift. Figure 3.4a shows the fringe position expressed as a phase offset for sequentially recorded images in a thermalised setup. Temperature variations change the refractive index of the fibres. A path delay of a single oscillation is sufficient to shift fringes by one period.[1] Fringe shift is always determined modulo $2\pi$. The figure shows jumps of $2\pi$ in the determination of the phase around frame 20 and 30 as a result of this modulo. From the image fringes shift over one full

[1]The effect of heat on the path delay is easily demonstrated by placing a heat source near a fibre. Fringes will shift several periods. This was first observed by Nik Noest.

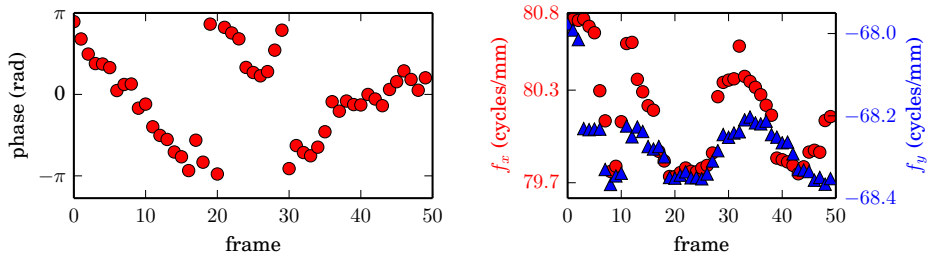


(a) phase drift (b) frequency drift

Figure 3.4: Probe function characteristics drift for sequentially recorded images in a stable thermalised setup.

period as a result of natural drift occurring in the time it takes to record 50 images. Therefore the thermal drift is used to shift diffraction patterns. No additional active shift mechanism is required.

Figure 3.4b shows the central fringe frequency for sequentially recorded images. A cause of the fringe frequency variation is the vibration of unsupported bare fibre. For probe reconstruction, the central fringe frequency cannot be considered constant if the variation on the fringe frequency is larger than one full period over the illumination region. Sometimes thermal variations do not cause a full period drift or fringe frequency variation is rather large. In those cases, python scripting allows for direct analysis of the recorded diffraction patterns. Thanks to the analysis, a decision to keep or reject the measurement can be made immediately.

### 3.2.4 Lensless magnification and resolution

A parabolic wavefront is created from the fibre tips. As a result the beam diverges as it propagates from the object to the camera. The diffraction pattern is recorded magnified by the camera, [15], see section 2.4.3. This is a very useful property as a telescope cannot be build without optics and pixels are generally bigger than half the period of the transmitted spatial resolution. Ray optics [29] can calculate the magnification using two similar triangles both having one point at the fibre tips and the opposite edge at the object and camera plane respectively. The magnification is then the ratio of the triangles. As discussed in section 2.1.3 the resolution decreases as the distance from the camera to the object increases. So for maximal resolution, the sample must be placed close to the camera. If additionally lensless magnification is desired, the fibre tips must be placed close to the object as well. This combination requires the setup to be very compact.

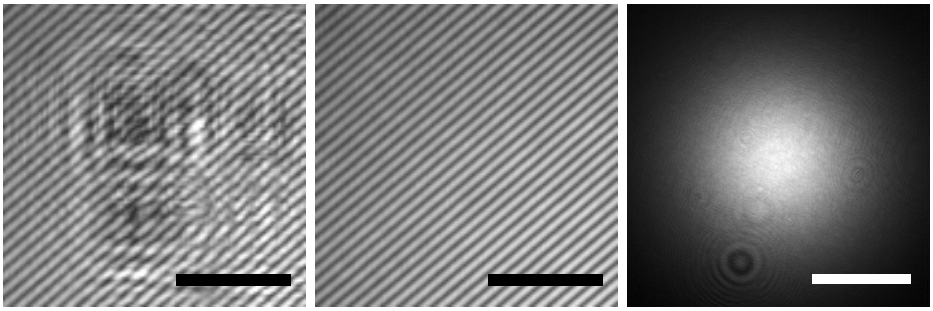

(a) thumbnail diffraction pattern of group 6, element 1 of a USAF resolution test target. [30]. Bar is 100 $\mu m$.

(b) The probe function of the area shown in figure 3.5a. Bar is 100 $\mu m$.

(c) Gaussian intensity distribution of a single beam. Bar is 500 $\mu m$

Figure 3.5: Images recorded during data collection. See appendix B for large scale images of measurement and reconstruction data.

## 3.3 Data collection

After alignment, firstly both arms of the interferometer have the same length, such that coherence is optimal. Secondly, the intensity of both arms is fairly equal to create a good modulation contrast. Thirdly, in case of reconstruction using straight fringes, free space propagation distance is also equal. A data set can now be acquired. The data acquisition can be scripted using python libraries[2]. This is important as it minimises the number of operations required to do a measurement and helps to standardize and improve quality of data sets. A data set contains

- Multiple diffraction patterns of the object. Usually 50 images are recorded in order to cover a full period drift, see section 3.2.3. Figure 3.5a shows a thumbnail of a captured diffraction pattern.

- A probe reference measurement. The sample is shifted to an empty area on the sample in order for the light to have the same optical path length. This image is needed for the probe reconstruction. Figure 3.5b shows a thumbnail of a recorded probe. The image shows straight fringes and an intensity gradient.

- The image of each interferometer arm separately. That is, with the other beam blocked and without interference. This data is also necessary to reconstruct the probe. Figure 3.5c shows a full size image of the Gaussian intensity distribution of a single probe beam.

[2]Credit goes to Marco Konijnenburg for writing a python c wrapper for the IDS camera.

- A background image, to be used for background substraction. This is particularly important if the camera is operated in rolling shutter mode, since in that case the background is uneven.
- A single beam diffracted image of the object. This data is used to easily determine the back propagation distance discussed in section 2.1. In principle this is also possible with a striped probe function illumination, however here it is much harder to recognize sharp structures.

# Chapter 4

# Results

## 4.1 Introduction

In order to demonstrate the results of interferometric illumination ptychography, first the ingredients necessary for image reconstruction are demonstrated. The propagation ability of the OTF will be shown by finding the correct back propagation distance to refocus a diffracted object. A probe reconstruction is shown and inspected. Next, the performance of interferometric illumination ptychography has been tested on a usaf 1951 [30] test target to determine the resolving capabilities of the system. Furthermore, cells of a plant stem have been imaged to test applicability to biological samples and investigate the capability to recover phase information. Both samples have been imaged using straight and curved fringe illumination. A post-reconstruction technique is shown that may be incidentally useful.

## 4.2 Back propagation distance

The reconstruction algorithm needs the back propagation distance $z$ to transform from the object domain to the measurement domain, see equation 2.9. Although the phase information is missing from the camera images, an intensity image can still be used to find the back propagation distance. Figure 4.1 shows an intensity image at propagation distances $z$. Features will become recognizably sharp at the right back propagation distance. No method exists to recognize sharp features automatically yet, so this step must be performed manually.

## 4.3 Goodness criteria for probe reconstruction

Goodness criteria can be used to determine whether the reconstructed probe fits the object diffraction pattern. Only the intensity is measured and therefore the reconstructed probe can only be compared with the intensity value

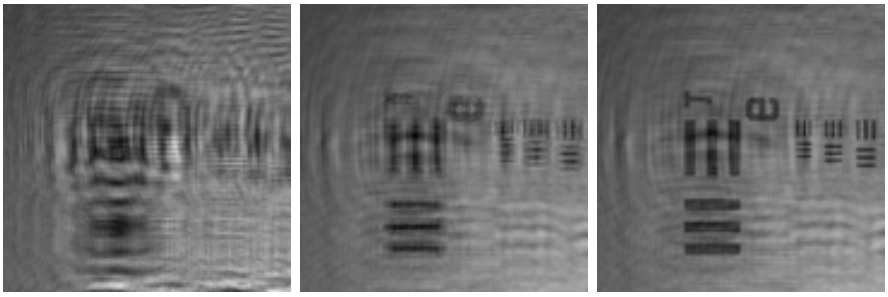

(a) Diffracted image. (b) Almost sharp. (c) Sharp.

Figure 4.1: The electric field amplitude image is back propagated and manually inspected to find the back propagation distance $z$. (a) no back propagation (b) image almost in focus at $z = 1.8mm$, (c) sharp at $z = 1.91mm$. Group 6 element 1 as well as group 7 elements 4 to 6 from the USAF target [30] are shown.

of the electric field. Thus the goodness criteria are insensitive to the phase of the reconstructed probe function which can be considered as a drawback. Two methods are used to judge the goodness of the reconstructed probe. The first method uses the normalised inner product

$$c\{\vec{f}, \vec{g}\} = \frac{\vec{f} \cdot \vec{g}}{\|\vec{f}\| \|\vec{g}\|} \tag{4.1}$$

as a goodness criterion, where the measured intensity and the probe function intensity are used for $f$ and $g$. The normalised inner product will never be unity as the diffraction pattern differs from the probe function by the object.

A second way to test the goodness of the probe reconstruction is by visual inspection of the difference between the diffraction pattern and the probe. Figure 4.2 shows a visual inspection of the goodness of a probe reconstruction. The difference of the reconstructed probe and the diffracted object is very close to zero for all places, except if the diffraction pattern of an object is present. Occasionally, probe reconstruction fails in certain areas. Visual inspection immediately makes this insightful.

## 4.4 Object reconstruction

If probe reconstruction is successful, the object can be reconstructed. For reconstruction a sequence of images is selected such that they have a linear increase in fringe phase and the reconstructed probe has a high goodness criterion $c$, equation 4.1. Usually 10 images are selected. These are then used in the reconstruction algorithm described in section 2.3.2. Figure 4.3 shows the application of a constraint during an iteration cycle . The object guess is

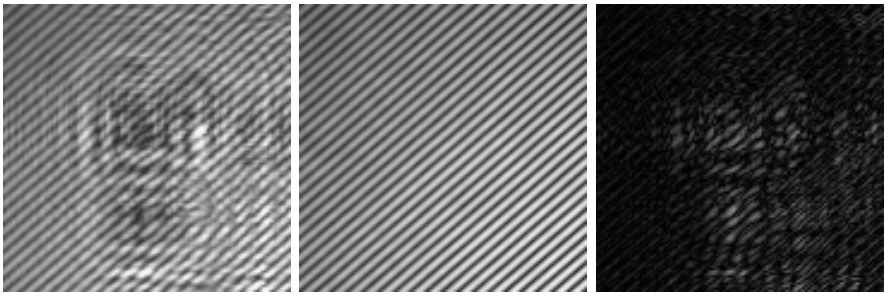

(a) Diffraction pattern. (b) Reconstructed probe. (c) Difference of 4.2a and 4.2b.

Figure 4.2: Visual inspection of the probe function reconstruction. (a) diffraction detail of group 6 element 1 of the USAF target. (b) reconstructed intensity probe function. (c) difference of (a) and (b).

transformed to the measurement domain, where the amplitude constraint is supplied. The applied constraint influences the object guess after it has been transformed back. The update of the object guess often follows a striped pattern as can be seen on the top-right of the image.

### 4.4.1 Convergence

As a measure for convergence the normalised inner product equation 4.1 for two consecutive iterations can be taken. If this comes close to unity it is an indication that the current object guess is stable. The convergence is shown in figure 4.4a. It is clear that for this measurement object guesses become increasingly alike. Additionally the convergence criterion shows a 10 cycle repetitive shape, this is related to 10 images being used for reconstruction. There will always be some difference between iterations as noise is not accounted for in the model and will thus be included in the object guess.

### 4.4.2 Post filtering

Often a reconstructed image shows residual fringes. This is often due to an error in the estimation of the fringe modulation estimation. Additionally fringes need many iterations of the algorithm to disappear, while the object otherwise has taken shape. Figure 4.5a shows a reconstruction result after 30 iterations. All objects are recognisable, but the reconstruction shows residual fringes. Residual fringes can be filtered by masking out the fringe frequencies in Fourier space. Fringes appear in localised places in Fourier space due to their well defined fringe frequency. The absolute value of the electric field is used in reconstruction. When the absolute value is taken negative values are flipped, creating discontinuities in the signal. Multiples of

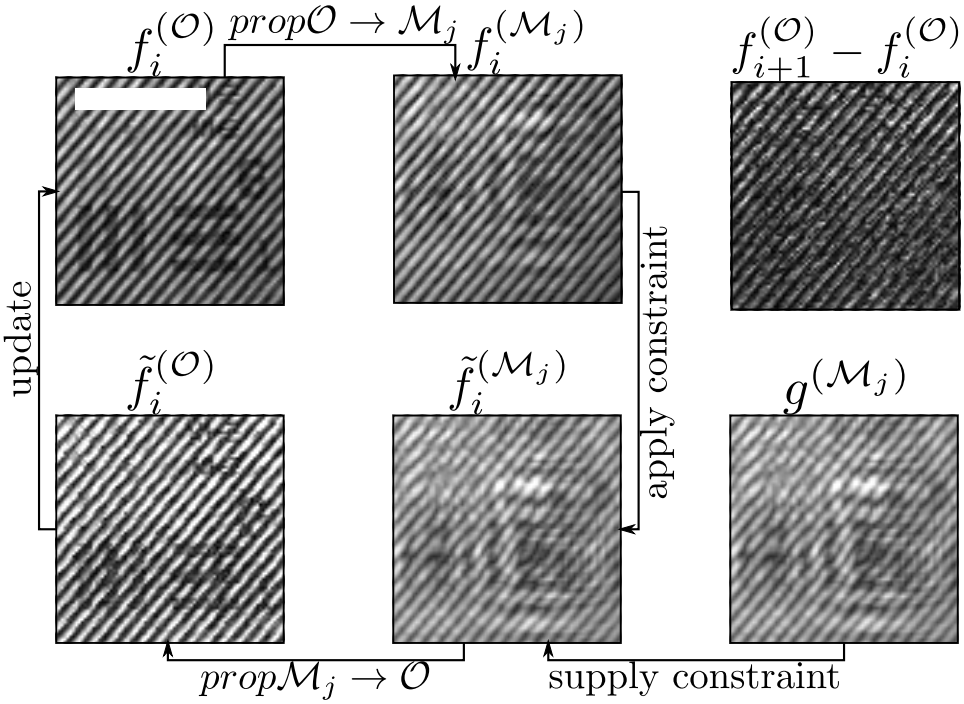


Figure 4.3: The fourth iteration cycle of a Gerchberg type reconstruction detailed in section 2.3.3. The object guess still shows a striped pattern which will disappear in later iterations.

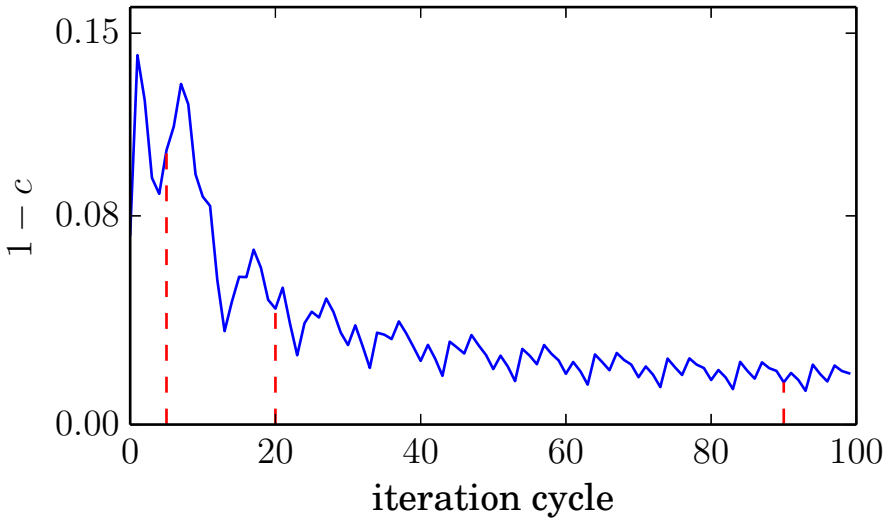


(a) Convergence for subsequent iterations. $c$ denotes the normalised inner product from subsequent iterations, see equation 4.1.

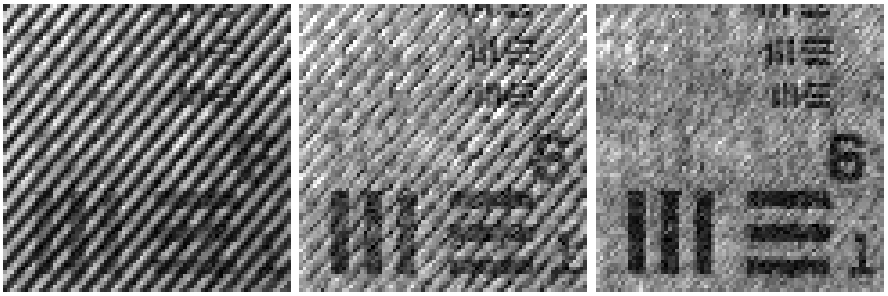

(b) Frame 5. (c) Frame 20. (d) Frame 90.

Figure 4.4: (a) convergence behaviour for reconstruction with 10 diffraction patterns. Red-dashed lines indicate the frames shown in (b-d).

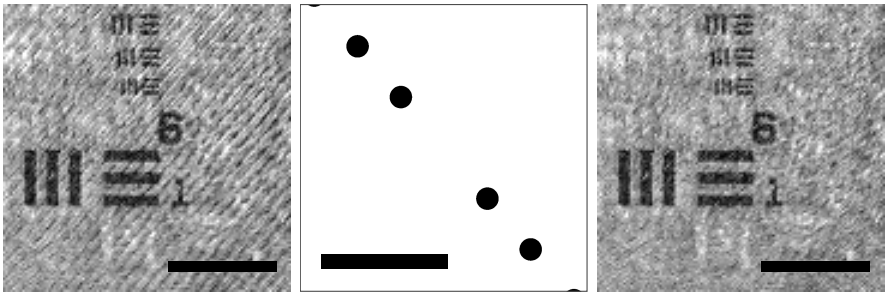

(a) Unfiltered, bar is $100\mu m$.

(b) Fourier mask, bar is 100 cycles / mm.

(c) Filtered, bar is $100\mu m$.

Figure 4.5: Post-reconstruction filtering. (a,c) detail showing group 6 element 1 and group 7 elements 4 trough 6 with and without post filtering. (b) Fourier space mask. Colour scale white: 1, black: 0.

the fringe frequency are required to describe the discontinuities. As a result, residual fringes appear in Fourier space as peaks at any integer multiple of the fringe frequency. Figure 4.5b shows a mask that can be used in Fourier space to filter out residual fringes. This post-filtering technique can be used to remove residual fringes after reconstruction or even reduce calculation times. Figure 4.5c shows the result of post-filtering a reconstruction after 30 iterations. It is not advisable to use this filtering technique however as the clipped frequencies also contain information on the image. This loss of information induces artefacts that deteriorates the image. For example, objects with spatial frequencies contained by the mask are now invisible after reconstruction. Additionally, a discontinuity in Fourier space also affects the smoothness in real space. Caution is advised when implementing this filter.

## 4.5 Image reconstruction for straight fringes

The probe function showed significant instability in the initial state of the experiment. Software was available to reconstruct unstable fringes under the condition that the fringes are very straight, see section 2.4.1. Results achieved with this technique are detailed below.

### 4.5.1 USAF target

The result of the usaf 1951 target reconstruction is shown in figure 4.6c. Elements of this reconstruction are used as illustrations throughout the thesis. The measured probe function used in this reconstruction is shown in figure 4.6a. Groups 6 and 7 from the usaf target are shown in figure 4.6b. Figure 4.2 shows a detail of a reconstructed probe and the corresponding difference

with the diffraction pattern. Firstly, from the reconstructed image it can be immediately seen that all groups are reconstructed sharp. Secondly, little evidence of shadow images remains. Thirdly, the image shows very little residual fringing. No post-filtering has been applied to achieve this image. The lensless magnification is obtained from a measurement of the largest structures visible in the image. The length of bars in group 4 element 1 is determined to be $93 \pm 1$ pixels. This corresponds to a physical length of $204.6 \pm 2.2\mu m$. From literature the length of the bars is exactly 156.25 $\mu m$. The lensless magnification is now taken from the ratio of the two. It is determined $M = 1.309 \pm 0.014$

From comparison of the reconstructed object and the probe measurement it can be seen that reconstruction is possible also for areas with relatively low illumination intensity. The background of the image is rather noisy, to quantify this the histogram of an area with sufficient illumination is taken and shown in figure 4.7. From the image of the theoretical object it is clear that the object is binary; either light passes undisturbed or it is absorbed completely. The histogram shows a double peak, a high peak at high pixel value indicating that the majority of pixels are white and a lower peak for lower pixel value belonging to areas filled with black bars. Both peaks are quite broad where for the theoretical object they would be very sharp. This indicates that there is significant noise on the image.

The inset in figure 4.6c shows the smallest bars available in the object, from the image it is not clear if also these smallest structures can be resolved since there is a lot of noise on the pixels. To determine the resolving power of this imaging technique 5 rows of pixels indicated by the letter b in the image have been averaged over, reducing noise while maintaining the resolving properties of the instrument, the result is shown in figure 4.8. The theoretical position and width of the bars shows that often a single pixel is partly covered by a bar. This reduces the contrast of the pixels. The Rayleigh criterion for resolution may be used to judge resolvability [31]. According to this criterion, two sources are resolved if the intensity midway the two sources is 0.735 the intensity at the source.[1] Resolution loss due to pixelation and noise are also accounted for with this criterion. Clearly, the intensity at the position of all bars is lower than 0.735 of the bright areas. Therefore the maximum demonstrated resolution is the width of the smallest bar, 2.2 $\mu m$.

The usaf is not a phase sample, so the reconstructed phase is expected to be flat. Figure 4.9 shows a detail of the reconstructed phase. The phase image shows the outlines of element 2 and 3 of group 6 on the usaf target. The background is zero with some residual stripes and noise. The amplitude of the electric field is close to zero wherever there is an object. If the ampli-

[1] The rayleigh criterion was initially developed to test the resolvability of two airy disks. However it is general enough to also provide a reliable measure in this case.

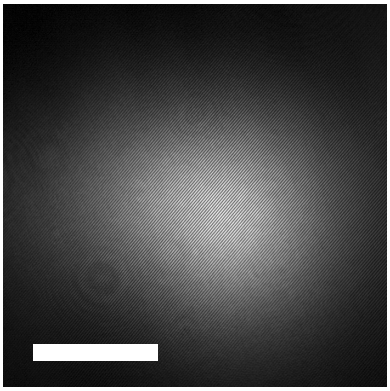

(a) Probe function intensity measurement used in reconstruction, bar is 0.5 mm.

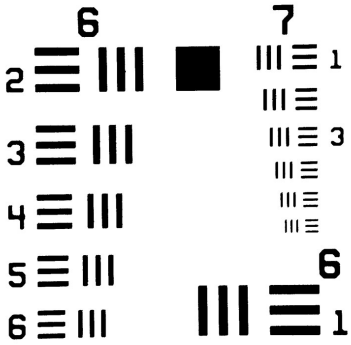

(b) Picture of smallest two groups of usaf target. Image taken from Thorlabs, Inc. website.

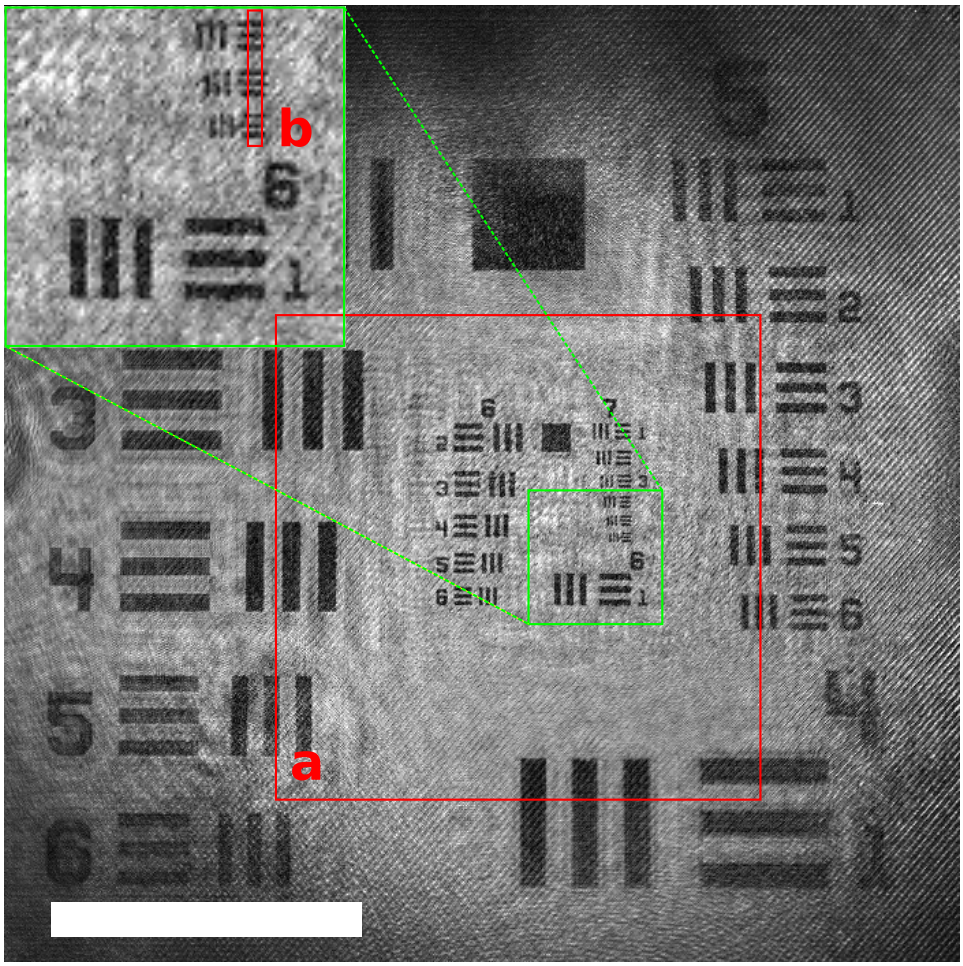


(c) Object guess of usaf target after 100 iterations. Area a indicates the area taken for the histogram. Area b indicates the area which is inspected to determine the highest resolution, the short axis is summed over to decrease noise. Bar is 0.5 mm.

Figure 4.6

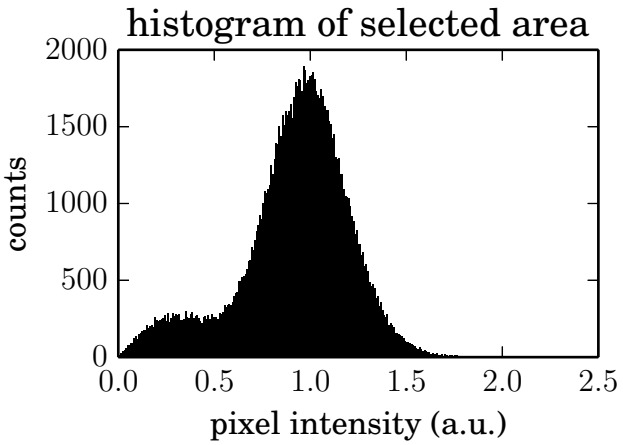


Figure 4.7: Pixel value histogram of area denoted with a in figure 4.6c. The object has only black and white values while the histogram of the reconstructed object shows broad peaks, indicating the noisiness in the reconstruction.

tude is close to zero the phase cannot be determined accurately. Therefore phase variations in the reconstruction of the usaf target may be considered a result of a numeric artifact rather than have a physical interpretation.

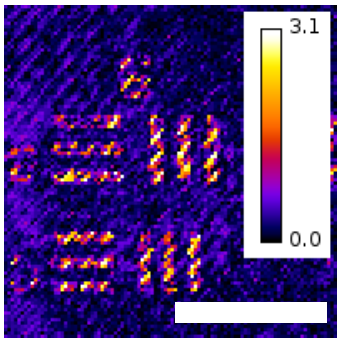


Figure 4.9: Detail of phase reconstruction for USAF target. Low electric field norm areas have varying phase. Bar is 100 $\mu m$, colourbar from to $\pi$ radians.

### 4.5.2 Biological sample

A biological sample is imaged to test the phase imaging capabilities as well as the performance of this imaging technique on more complicated samples. The stem of a sea anemone is used as a sample. The result of the reconstruction is shown in figure 4.10a. An image recorded with a widefield optical microscope is shown in figure 4.10b. Part of the image is dominated by noise and structures can not be clearly distinguished. Other parts can be reconstructed to recognizable shapes, here also the contrast is rather low and the image is quite noisy. Considering this it can be said that the reconstruction is not very successful. The low contrast may be explained by considering that the biological sample scatters light more weakly, i.e. not so much light is scattered by the object or the signal from the object is not so strong. In the presence of noise it is difficult to distinguish shapes.

Visual inspection of the reconstruction of the probe function may explain some of this behaviour. As discussed in section 4.3 the difference between a measured diffraction pattern and the reconstructed probe should be the signal generated by the object. The difference is shown in figure 4.10c, there is a large band which shows a striped pattern clearly not originating from the object. From this it is clear that the probe reconstruction failed in some areas and that these areas become noisy in the reconstruction result.

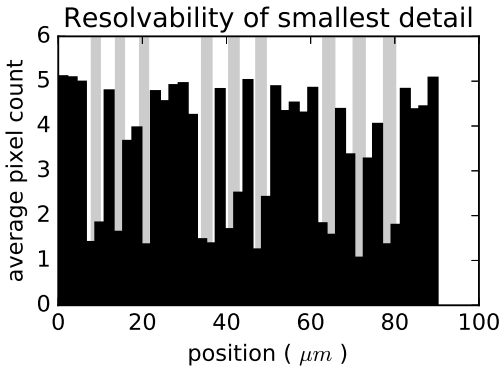


Figure 4.8: Resolvability of 3 smallest sets of bars. Five rows of pixels along the length of the bars have been averaged over to reduce noise. Grey bars indicate the theoretical position and width of the bars, based on literature and measured lensless magnification. For even the smallest bars there is clear separation between bright and dark areas.

An important goal of ptychography is to do phase imaging. The USAF target is a binary target and thus exhibits no phase behaviour. Figure 4.11 shows a detail of the reconstructed phase of the biological sample. Similar to the reconstruction of the usaf target the phase reconstruction for the biological sample shows phase variations in places of low electric field amplitude. The phase image outlines cell walls. The same cell walls are also visible in the amplitude reconstruction as low amplitude areas. Phase reconstruction of the usaf sample has demonstrated that phase reconstruction in low amplitude areas is random. Considering the overlay of low amplitude and phase variations in the biological sample, it is possible that the reconstructed phase variations are induced by amplitude variations. Additionally, a sample of several tens of microns thick may scatter the incoming blue light several times [32]. In conclusion it is not possible to demonstrate phase imaging from this reconstruction: phase reconstruction may have failed for this object, or the object may not be suitable for phase imaging.

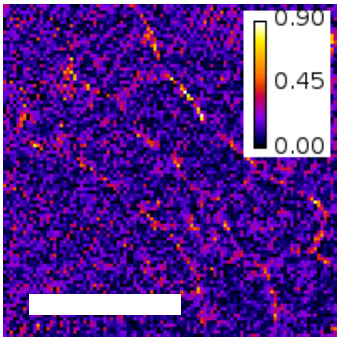


Figure 4.11: Detail of phase reconstruction for biological sample. The phase outlines cell walls and shows no further structures. Bar is 100 $\mu m$.

## 4.6 Image reconstruction for curved fringes

At a later stage in the experimental development, several experimental improvements were made to improve the stability of the probe function. Firstly the bare fibres were taped to mounts for a long stretch for pull relief. Secondly the bare fibre extends only a few millimetres in free space to reduce vibrations. Lastly the FC/PC fibre sleeves were no longer used to compensate for unequal fibre lengths. Fixed fibre sleeves also allow also for much better control over the relative intensity of the branches. However, the path

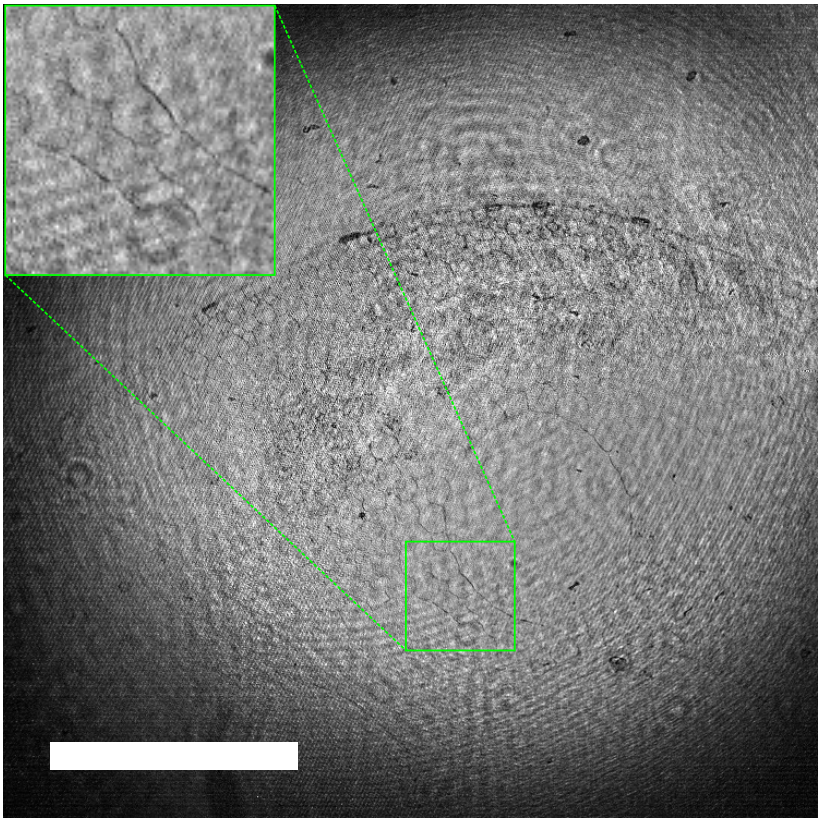

(a) Reconstruction of stem of sea anemone using straight fringes. Reconstruction shows a very noisy signal. Some areas of the image are completely dominated by noise. The inset shows a detail of the image, also shown in a reference widefield image shown in 4.10b. Bar is 0.5 mm.

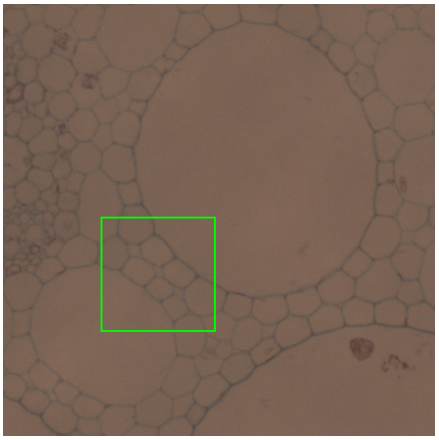

(b) Optical Widefield microscope image of sample detail. Green box indicates area of detail.

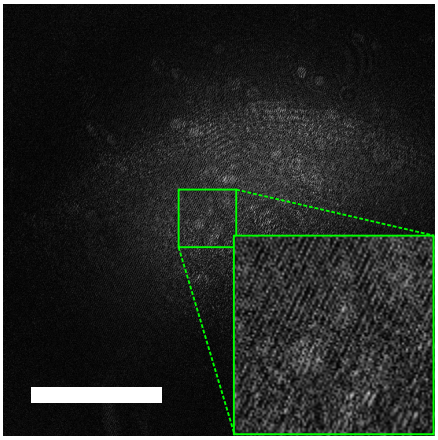

(c) Difference of probe and diffraction shows striped residu indicating flaws in the probe reconstruction. Bar is 0.5 mm.

Figure 4.10

length of both arms needs to be equal for coherence. Unequal fibre lengths lead can be compensated for with unequal free space propagation, which in turn leads to curved fringes. A new probe reconstruction method for stable curved fringes was developed, see section 2.4.2. Furthermore, a Gaussian filter was implemented into the algorithm to suppress noise from image reconstruction. The results are shown in this section.

### 4.6.1 Usaf target with curved fringes

Figure 4.12 shows a reconstruction of the usaf target for curved fringes. The reconstruction successfully reconstructs large scale structures and shows little artefacts over a large field a view. Figure 4.13 shows a part of the diffraction pattern as well as the difference of the diffraction pattern and the reconstructed probe. The latter image clearly outlines diffraction patterns of the objects, whereas fringes in empty areas of the object are almost completely suppressed. This behaviour is visible over the entire range of the reconstruction (not shown). An enlarged view of the central smallest structures as well as the effects of a Gaussian filter is given in figure 4.14. The lensless magnification for this recording is unity. As a consequence the smallest structures visible in the reconstruction are close to the Nyquist sampling frequency, see appendix A.3, limiting the resolution.

A histogram is used to inspect the noisiness of the image. A perfect reconstruction of a binary object shows only two very sharp peaks. A measure for the noisiness can be obtained from the variation around these peaks. For no Gaussian filtering the noisiness is comparable to the reconstruction using straight fringes of the usaf target, see figure 4.7. The peaks are recognisable as separate, however there is no minimum in between the two peaks. A Gaussian filter was implemented in the algorithm. Each iteration a relative weak filter was applied to the current object guess. This method aims to suppress random noise, as these are suppressed by sequentially applied filters. Signal is added again each iteration, such that it is suppressed only very weakly. For a balanced filter with a standard deviation of a half with respect to the pixel size, the histogram shows a clear minimum between the peaks. Stronger filtering with a standard deviation of a pixel mostly sharpens both peaks. A Gaussian filter may also improve resolvability through noise suppression. Structures are more clearly recognisable in case of medium filtering. A set of bars is considered resolved if all six bars, horizontal and vertical, of an element can be recognised individually. Element 2 of group 7 is the smallest element where this is still possible, corresponding to a bar width of 3.5 $\mu m$. Stronger filtering reduces noisiness, but also blurs structures. Therefore, a suitable standard deviation for the Gaussian filter is determined to be around half a pixel.

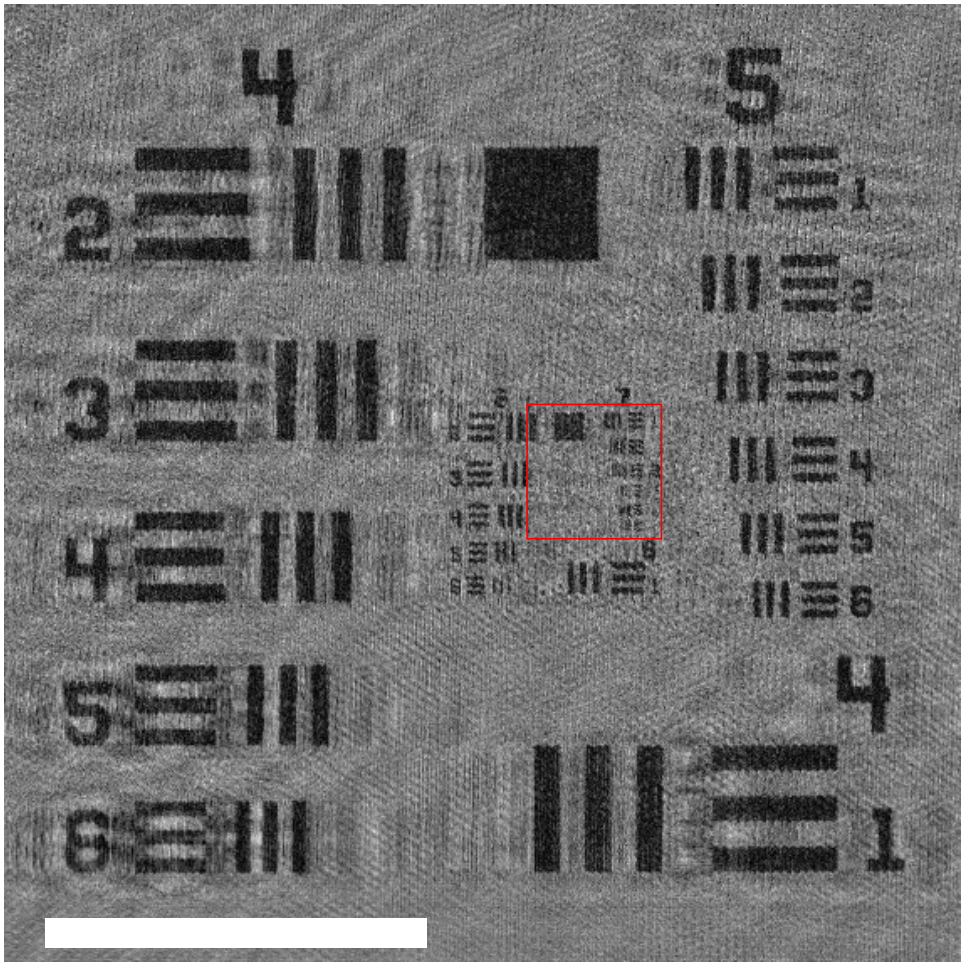


Figure 4.12: Reconstruction of usaf 1951target with curved fringe illumination. Groups 4 to 6 are shown. Element 2 of group 7, corresponding to a bar width of 3.5 $\mu m$ is the smallest resolvable element. This can be seen from the enlargement of the red box in figure 4.14. The lensless magnification is effectively unity, significantly smaller than the result of figure 4.6c. Bar is 500 $\mu m$.

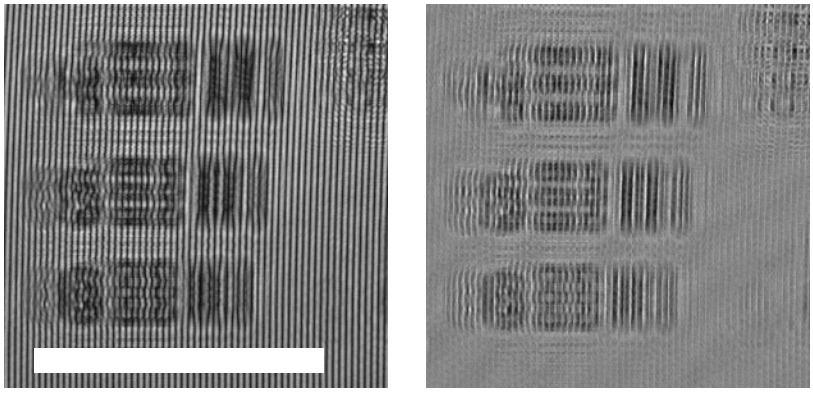

(a) (b)

Figure 4.13: Probe reconstruction for curved fringes illuminating the 1951 usaf target, elements 4 to 6 of group 4 are visible as well as elements 4 to 6 of group 6 in the top-right corner. (a) shows a measured diffraction pattern displayed as the norm of its electric field. (b) shows the difference between the measured diffraction pattern and the reconstructed probe. The residu is clearly recognisable as diffraction patterns and very little fringes remain. Bar is 500 $\mu m$, the scale is equal for both images.

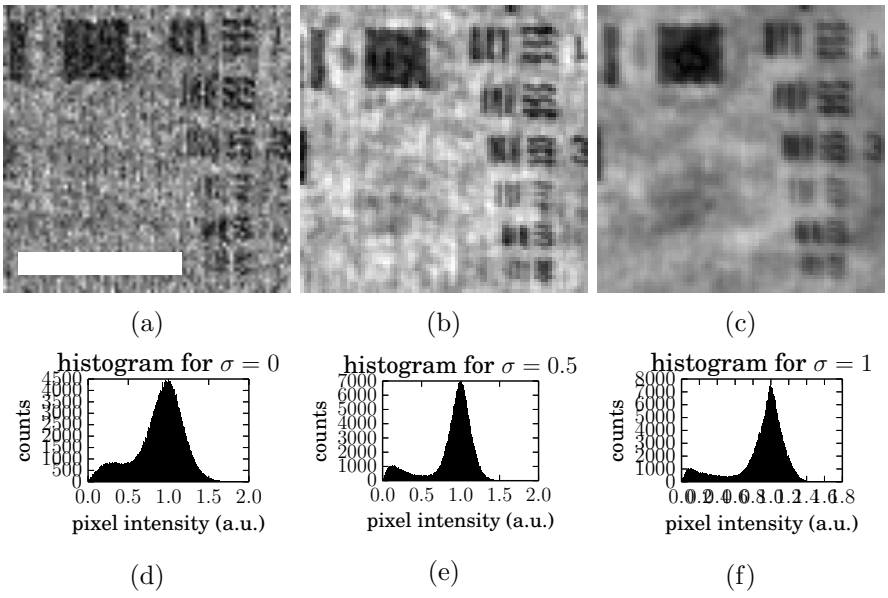


Figure 4.14: Results of a Gaussian filter implementation in the reconstruction algorithm. The usaf target is a binary object. Therefore, the width of the two peaks in the histogram is an indication of the noise present in the image. The standard deviation $\sigma$ relates to the width of a pixel. (a,d) No filtering. (b,e) medium filtering for $\sigma = 0.5$. (c,f) heavy filtering for $\sigma = 1$. Bar is 100 $\mu m$, the scale is identical for (a-c).

### 4.6.2 Biological sample with curved fringes

A second reconstruction of the biological sample was performed using curved fringes and a $\sigma = 0.5$ Gaussian filter. It was hoped that under more stable circumstances, also the more challenging biological sample can be imaged. Surprisingly, the phase of the reconstructed object allows for the best interpretation of the image as its shows the least noise. Figure 4.15 shows a large scale image of a sea anemone stem also imaged in 4.10a. Cell walls as well as dark speckles are clearly resolvable over the entire field of view. It is unclear what the black speckles are, they might simply be specks of dirt trapped in the sample during preparation. The phase reconstruction shows concentric rings around the top-left corner. These rings are also visible in the probe reference measurement shown in figure 4.15b. The probe reference is measured by recording an ampty part of the sample. However, for this sample all areas contain at least a small amount of dirt, limiting the quality of the probe reference measurement.

The phase reconstruction shows large scale phase variations at the bottom of the image. Figure B.8 in appendix B shows the difference of the reconstructed probe and the measured diffraction pattern. Large areas in the image show significant fringing. It is remarkable that image reconstruction is successful in placed with large residual fringing. A solution can be found from the large scale phase variations in the reconstructed object. These variations cause fringes to shift with respect to a reference measurement, creating residual fringing. Earlier attempts at reconstruction of this biological sample were unable to arrive at a solution with large scale phase variations. Instead, areas with residual fringing were reconstructed badly.

A numerical artefact is visible in the top part of the reconstruction. This is a consequence of the periodic boundary condition of discrete Fourier transform: as a numerical propagation is performed, parts of the structure diffract outside of image. Due to the periodic boundary condition, the diffraction pattern enters the image from the other side. This creates interference and noise, see section A.3 for more information on properties of discrete Fourier transforms.

In figure 4.16 an amplitude and phase detail of the reconstruction is shown. The phase image again resembles the amplitude image closely. Contrary to the reconstruction from straight fringes, see section 4.5.2, image quality is now sufficient to recognise uninterrupted black structures as cell walls in the phase image. This is an indication that phase imaging is indeed possible. This hypothesis is supported by the phase image histogram in figure 4.15. If all low amplitude area would have a random phase, this would appear in the histogram as a noisy DC offset over the entire phase domain. This is clearly not visible in the histogram as the phase signal is almost completely limited within one radian considering the logarithmic scale. As a further indication of phase imaging, a bright spot is visible in the top right

of the phase reconstruction in 4.16. Whereas the bright spot is not visible in the amplitude reconstruction. Although the author has insufficient biological knowledge to predict the presence of optically active cells, the specificity of the shape and uniqueness in position indicate that the signal is caused by an object, rather than an artefact in reconstruction.

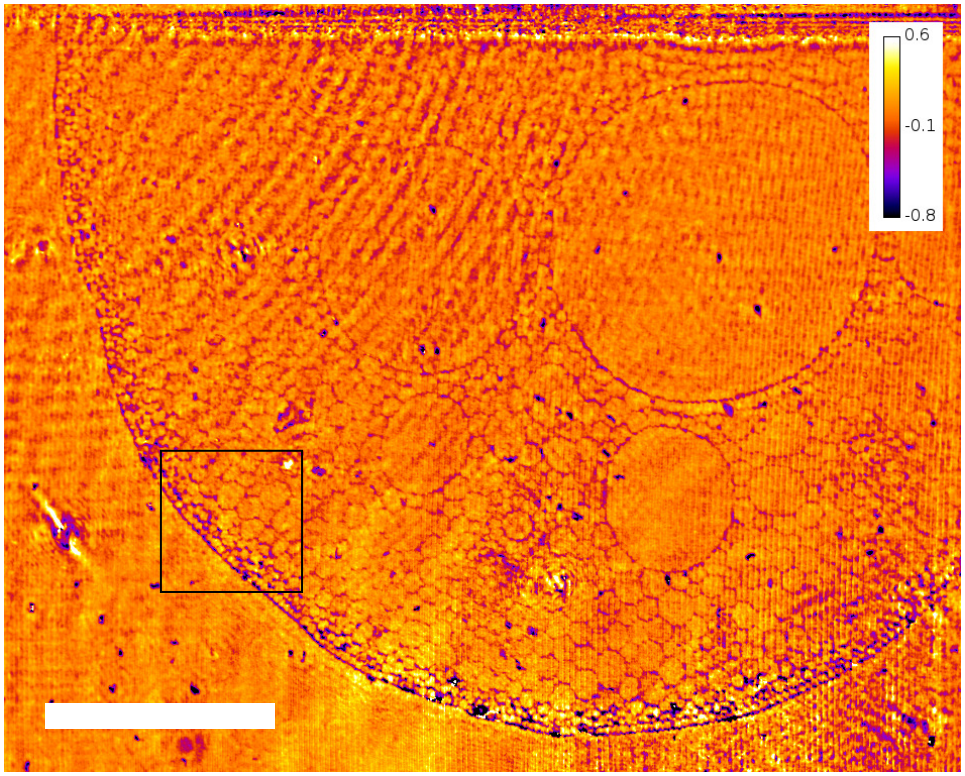


(a)

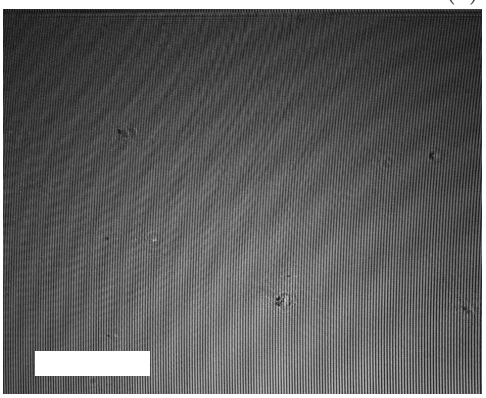

(b)

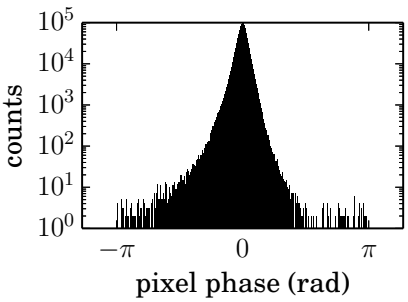


(c)

Figure 4.15: Reconstructed phase of a biological sample, obtained with curved fringe illumination and $\sigma = 0.5$ Gaussian filtering. (a) large scale image of the reconstructed phase of the stem of a sea anemone. Cell walls of various cells are clearly visible. A numerical artefact from propagation is visible at the top of the image. The black box is enlarged in figure 4.16. Concentric rings visible in the top-left corner are also visible in the electric field of the probe reference, shown in (b). (c) shows a histogram of the reconstructed phase. A single peak around zero phase is visible. Bar is 500 $\mu m$ for (a,b).

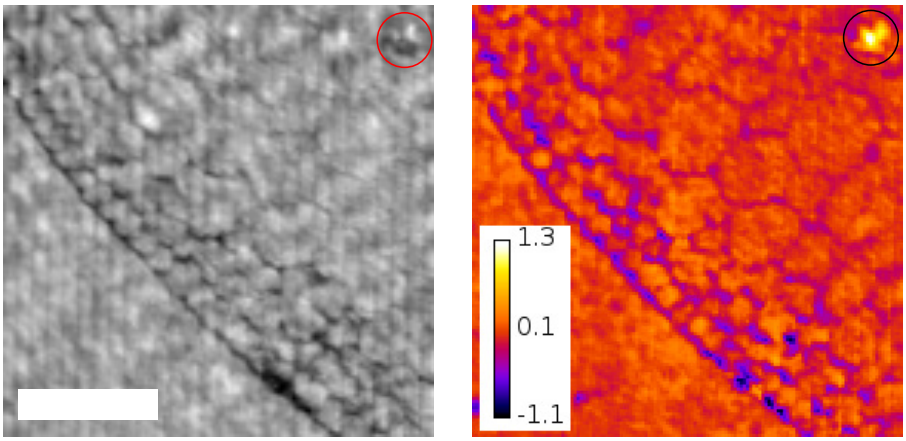


(a) amplitude (b) phase

Figure 4.16: Detail of sea anemone reconstruction using a $\sigma = 0.5$ Gaussian filter. (a) electric field amplitude. Individual cells are recognisable. The background shows significant large scale variations as well as a striped residu of the probe function. (b) the phase of the electric field. Noise is much less prominent and cell walls are clearly visible as solid lines. Cells in the interior show lower phase contrast, making them harder to distinguish. In the right (circle) an object with strong phase is visible. Bar is 100 $\mu m$. Scale is identical for both images.

# Chapter 5

# Conclusion and discussion

A ptychographical setup has been built and the tools to do reconstruction have been developed by others and enhanced by the author of this thesis. Tools for reconstruction include a method for back propagating, a probe reconstruction method and an object reconstruction method. A usaf resolution test target has been successfully reconstructed with a structure of 2.2 $\mu m$ still clearly resolvable. The resolution is limited by the pixel size of 2.2 $\mu m$. To investigate the theoretical limits of this imaging technique it is necessary to either increase the lensless magnification or get a camera with smaller pixel size. Successful reconstruction of a biological was possible after the development of a new probe reconstruction technique. Probes with curved fringes can now be reconstructed, allowing for a more mechanically stable setup. A stem of a sea anemone has been successfully imaged over a field of view of 2 mm. Cell walls are clearly outlined in the amplitude and phase image. Proof of the phase imaging capabilities of this system is given by the line quality of reconstructed cell walls, the limited domain of reconstructed pixel phase values and the appearance of objects in the phase image, that are not present in the amplitude image. These three observations indicate that structures visible from the phase reconstruction are actual and not a consequence of an undetermined phase in low amplitude areas. Several issues remain. Firstly, a biological sample of several tens of microns thick is likely to be bothered by multiple scattering [32] especially for short-wavelength blue light. Secondly, a biological sample influences the phase and the amplitude of the prove weakly. Signals resulting from noise or unwanted interference effects may be comparable in strength to signal from the image, hampering reconstruction. To investigate further, a sample with low thickness and multiple $2\pi$ phase variation may be imaged.

Presently, a robust imaging method is available with good control over experimental parameters. This can be used as a starting point for further development. In particular, the propagation distance from the object to the camera can be varied in a controlled way. The resolution is expected to

increase as more diffraction angles are captured by the camera. It is unclear however how the resolution increases as there is no Fourier transform relation between the object and the camera plane. A variation of propagation distance would give insight into this problem.

The current reconstruction result is rather noisy and this degrades the image quality. A Gaussian filter is introduced to reduce noise and as a result image quality improves. Contrary to the noisy reconstruction result, measurements of diffraction patterns and probe reconstructions are smooth. It may be worthwhile to investigate the noise enhancement properties of the reconstruction algorithm.

A large amount of literature [6, 24, 26] has been written on a variation of image reconstruction techniques. Several approaches for specific problems have been brought forward. By contrast, scientists in the field of coherent diffractive imaging (CDI) seem to prefer variations of the Gerchberg method in most cases [11, 16, 18]. It may proof useful to make a study of available literature and asses the possibility to implement available reconstruction literature in the field of CDI.

An important aim of this work is to pave the way for interferometric illumination ptychography using higher harmonic sources. This work shows the feasibility of interferometric illumination ptychograph. Several issues remain however. Reconstructed images are rather noisy even with a Gaussian filter and pixel size is a serious limitation on the achievable resolution in the Fresnel regime. To implement interferometric illumination ptychography for higher harmonics requires operation in vacuum, where experimental problems are more prone to appear. Probably it is useful to continue this experiment in the visible regime to solve for problems originating from the principle of interferometric illumination ptychography.

# Appendices

# Appendix A

# Theory for practical problems

## A.1 Light propagation in fibres

Single-mode optical fibres can guide light in an easy and flexible way. Only the lowest order mode can exist in a single-mode fibre. The lowest order mode is a Gaussian amplitude distribution with a flat phase profile. Upon entering free space, light is no longer contained in the fibre and will diffract. The diffracted light can be described by the focus of a Gaussian beam, with the focus located at the bare fibre exit.

Furthermore, fibres show stress induced birefringence. That is, the refractive index along a material axis changes as a result of the stress on that axis. So if a fibre is stressed by e.g. bending it, the polarisation of the light will change. Applying stress on a fibre in combination with a polariser is a useful way to attenuate your beam. For phase imaging, light must be in the same polarisation state to interfere. It is likely that stress induced birefringence occurs unintentionally while guiding fibres. This creates partly orthogonally polarised light. To be sure of identical polarisation in a fibre based interferometric setup, a linear polariser is advisable.

Lastly an optical fibre may leak light if the bending radius becomes very small. In this case light from the core of the fibre can couple to modes in the fibre cladding and leak out. In practice unwanted losses from bending are easily avoided and controlled bending provides an opportunity for attenuating fibre conducted light.

## A.2 Coherence

In an interferometer light from a single source is split into two pathways and then recombined. By changing the length of one pathway, it is possible to interfere light from the same source at two different points in time.

$$I(\tau) = \lim_{T\to\infty} \frac{1}{T} \int_0^T \big|E(t) + E(t-\tau)\big|^2 \mathrm{d}t \tag{A.1}$$

$$I(\tau) = \lim_{T\to\infty} \frac{1}{T} \int_0^T |E(t)|^2 + |E(t-\tau)|^2 + 2\,\mathrm{Re}\big[E(t)E(t-\tau)\big]\mathrm{d}t. \tag{A.2}$$

The Fourier transform of the intensity as a function of time gives the spectrum of the intensity. Additionally the integration time can be assumed to be much greater than the delay time $\tau$.

$$\hat{I}(\omega) = 2\,\langle E\rangle\,\delta(\omega) + 2\,\mathrm{Re}\big[E(\omega)^2\big]. \tag{A.3}$$

This states the well known results that the Fourier transform of an interferometer signal is the absolute autocorrelation of the spectrum of the light source. The third therm in the integral A.2 can be written as the product of a carrier frequency $\omega_c$ and a modulation function,

$$\lim_{T\to\infty} \frac{1}{T} \int_0^T 2\,\mathrm{Re}\big[E(t)E(t-\tau)\big]\mathrm{d}t. = C(\tau)sin(\omega_c\tau), \tag{A.4}$$

where the function $C$ can now be recognised as the *coherence function*. The shape of the coherence function depends on the spectrum of the signal. Often the coherence length is used as a characteristic length of the coherence function. This is useful if the coherence function is a well localised function such as a Gaussian. The definition of coherence length can be problematic if the coherence function is oscillatory as in the case of a laser lasing at multiple modes.

It may be intuitive to consider a heuristic argument for the coherence length of a Gaussian spectrum. The coherence of a Gaussian is also shaped like a Gaussian. Consider two frequencies separated by $\Delta\lambda$ and carrier wavelength $\bar{\lambda}$at full-width-half-max (FWHM) of the spectrum. Each period the two wavelengths go $\Delta\lambda/\bar{\lambda}$ out of phase and after they go a full period out of phase the signal becomes incoherent. So $\bar{\lambda}/\Delta\lambda$ cycles of length $\lambda$ pass before the signal becomes incoherent. The coherence length can be estimated as

$$L_c = \frac{\bar{\lambda}^2}{\Delta\lambda} \tag{A.5}$$

With $L_c$ the coherence length. For phase imaging the light source must be coherent section 2.2.1. For a $450\,nm$, $1\,nm$ bandwidth blue laser diode, this coherence length is in the order of $400\,\mu m$. For an interferometric setup

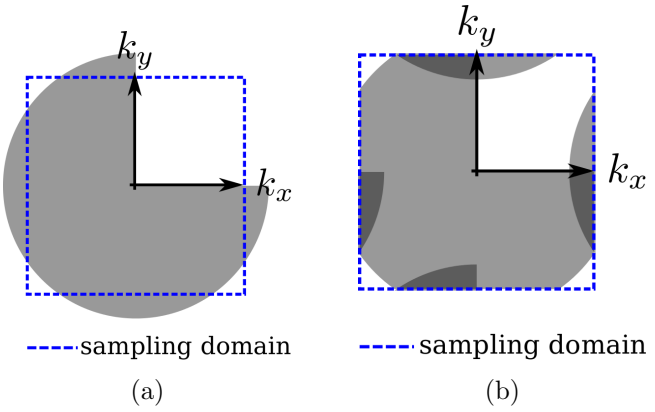


Figure A.1: Aliasing of a circular spectrum onto a rectangular sampling domain. (a) The theoretical spectrum has zero intensity in one of its quadrants to illustrate the shifting property. (b) The clipped intensities shift as if there are periodic boundary conditions. This is clear from where the zero intensity quadrant appears.

the coherence should be large and uniform over the path delay of the sample, from eqs. (A.2) and (A.3) the interferometric signal is the Fourier transform of the intensity spectrum, such that the length of large uniform interference is inversely related to the broadest structures available in the spectrum. If a laser is lasing at multiple modes, the effective bandwidth is the distance between the outer edges of the modes.

## A.3 The Nyquist criterion

The Nyquist criterion states that a Fourier component must at least be sampled twice each oscillation in order for it to be measured by a discrete detector. For some $\Omega$ bandwidth limited signal, the Nyquist distance is then half the period of $\Omega$. All information transmitted by the imaging system is digitalised if the sampling is done according to the Nyquist criterion. If the sampling is finer, the stored dataset is larger than it need be. If it is smaller information is lost due to *aliasing*. Suppose some sampling frequency $2\omega_s$, it is impossible to distinguish the sampled signal of $\omega_s + \delta\omega$ and $-\omega_s + \delta\omega$, this follows directly from

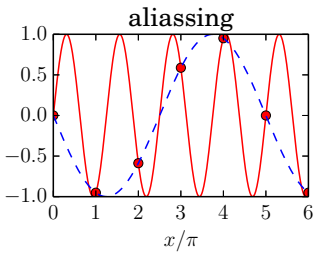


Figure A.2: Illustration of aliasing. Sampling a frequency $\sin(1.6x)$ (red) higher than half the sampling frequency results in it being reconstructed as a lower frequency $\sin(-0.4x)$ (blue, dashed).

$$\begin{aligned} \exp\big(\mathrm{i}2\pi(\omega_s + \delta\omega)x\big)\Big|_{x=\frac{n}{2\omega_s}} &= \exp\big(-\mathrm{i}2\pi(\omega_s - \delta\omega)x\big)\Big|_{x=\frac{n}{2\omega_s}} \\ -1^n \exp(\mathrm{i}\pi\delta\omega) &= -1^n \exp(\mathrm{i}\pi\delta\omega). \end{aligned} \tag{A.6}$$

The higher frequency is counted as a lower frequency and information is lost, see figure A.2. The spectrum shifts unto itself as if there where periodic

boundary conditions. The transfer function of a microscope is usually a circle due to cylindrical symmetry. On the other hand, most chips are rectangular and consequently the boundary frequency where aliasing occurs is a square. Figure A.1 shows the effect of aliassing in case a circular frequency signal is measured by a rectangular pixel grid.

## A.4 Derivation of Fraunhofer diffraction

Starting from the Fresnel diffraction equation 2.3, the Fraunhofer diffraction equation can be proven straightforwardly by expansion of therms under the assumption $z \gg k(x'^2 + y'^2)_{max}$.

$$E(x,y,z) = \frac{\exp\left(\mathrm{i}kz + \frac{\mathrm{i}k}{z}(x^2+y^2)\right)}{\mathrm{i}\lambda z} \iint_D \mathrm{d}x'\,\mathrm{d}y'\,E(x',y',0)\exp\left(\mathrm{i}k\frac{-xx'-yy'}{2z}\right)\exp\left(\mathrm{i}k\frac{x'^2+y'^2}{2z}\right). \tag{A.7}$$

In the Fraunhofer approximation the last phase therm in the integral generates an almost flat wave front and it can be ignored. The intensity is insensitive to phase offsets so the exponential before the integral can be ignored. What is left has exactly the shape of a Fourier transform

$$E(x,y,z) = C\iint_D \mathrm{d}x'\,\mathrm{d}y'\,E(x',y',0)\exp\left(\mathrm{i}k\frac{-xx'-yy'}{2z}\right), \tag{A.8}$$

where the prefactor has been named a constant C and the result shows a direct Fourier transform relation between electric fields at planes perpendicular to the optical axis.

# Appendix B

# Raw data

For the purpose of repeatability and completeness of results it is useful to include raw data of diffraction measurements. Furthermore the performance of probe reconstruction is also shown. Several issues may cause probe reconstruction to be faulty. In turn, faulty probe reconstruction is in many cases the cause of a failed object reconstruction. The success of a probe reconstruction can best be assessed by subtracting the reconstructed probe from the corresponding diffraction measurement.

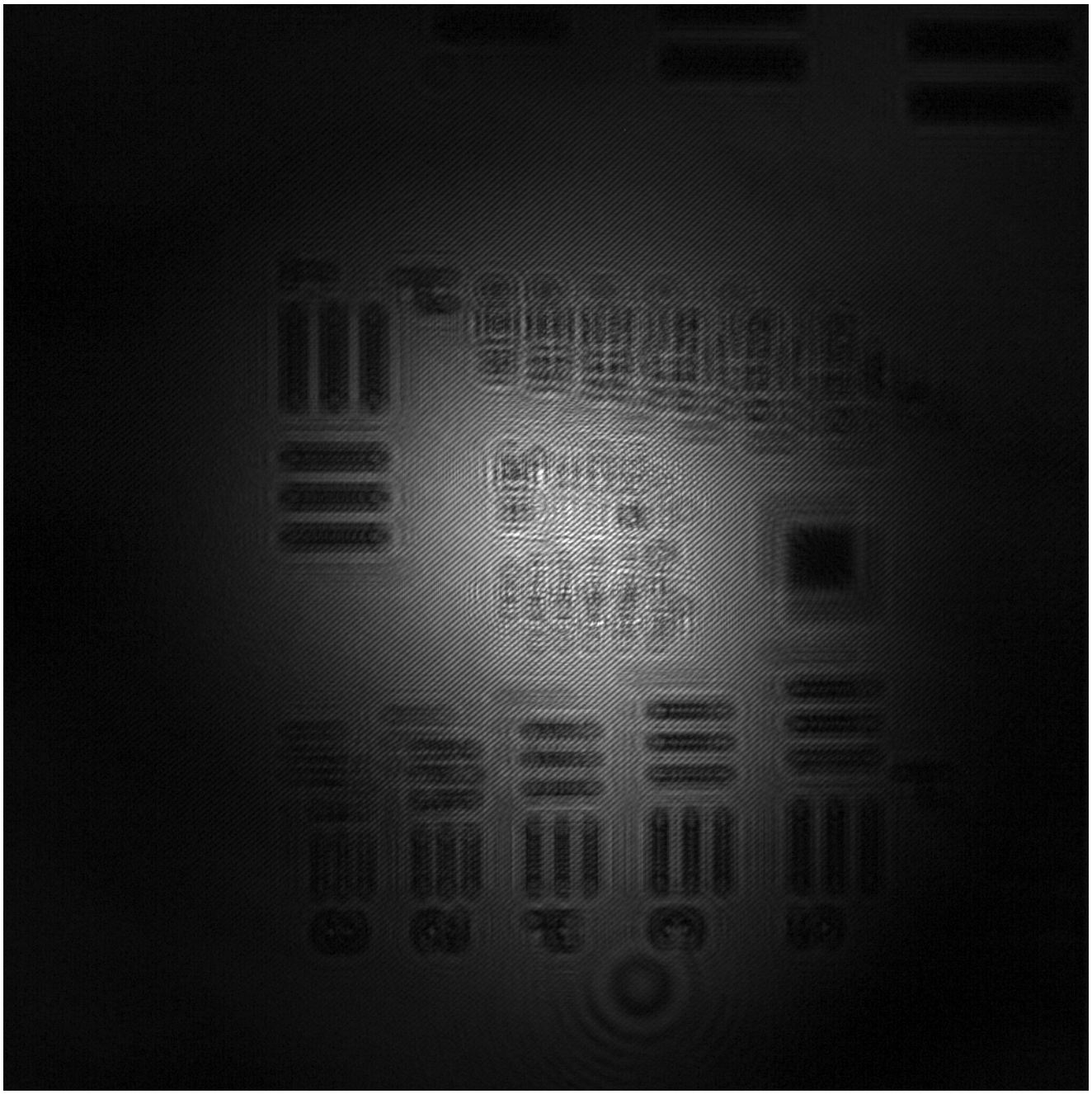

Figure B.1: Diffraction measurement for usaf 1951 resolution target reconstruction using straight fringes. See section 4.5.1 for reconstruction.

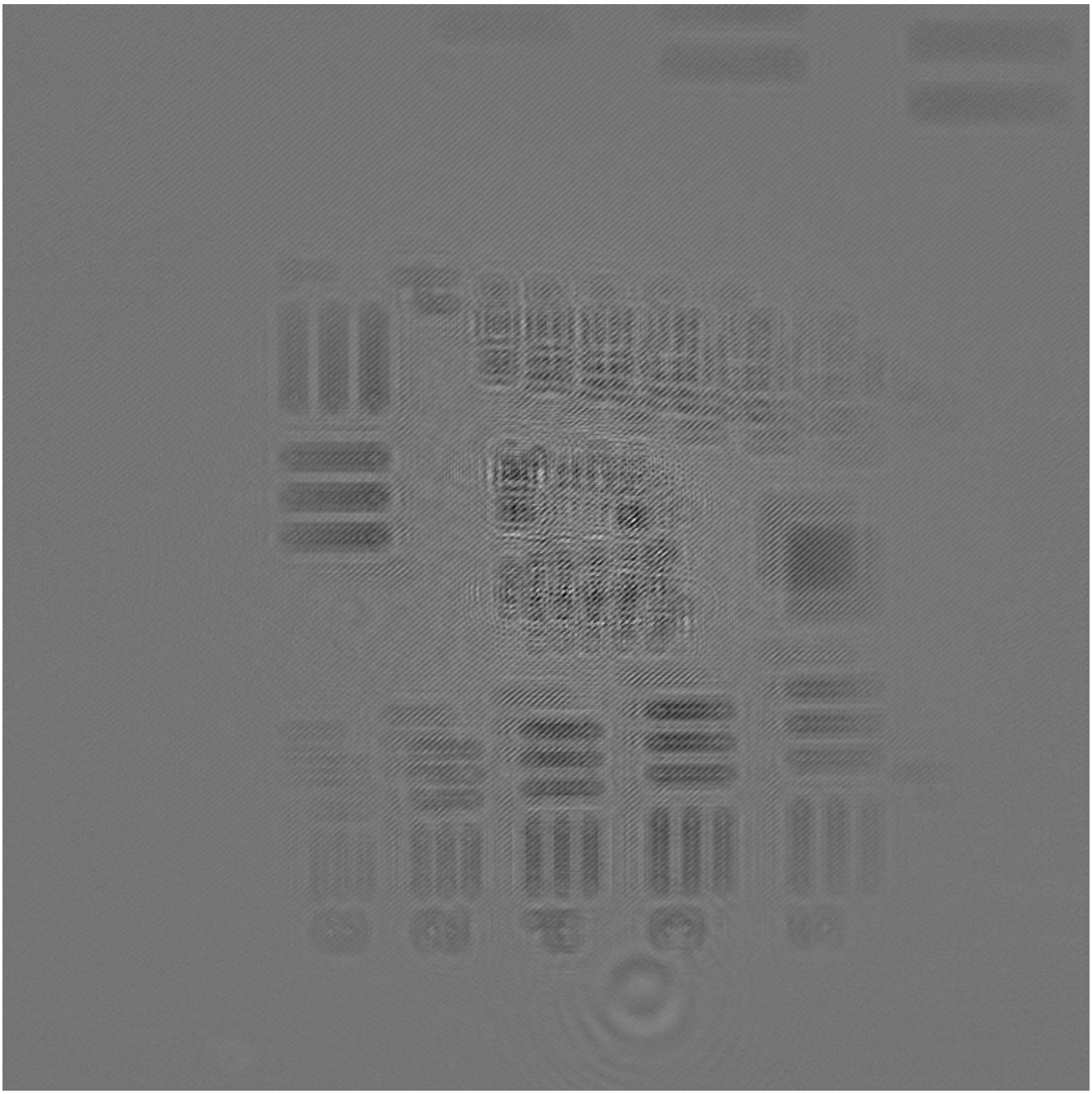

Figure B.2: Difference of reconstructed probe and measured diffraction pattern for usaf 1951 resolution target reconstruction using straight fringes. Reconstruction is almost completely successful. Low intensity residual fringing is visible. See section 4.5.1 for reconstruction.

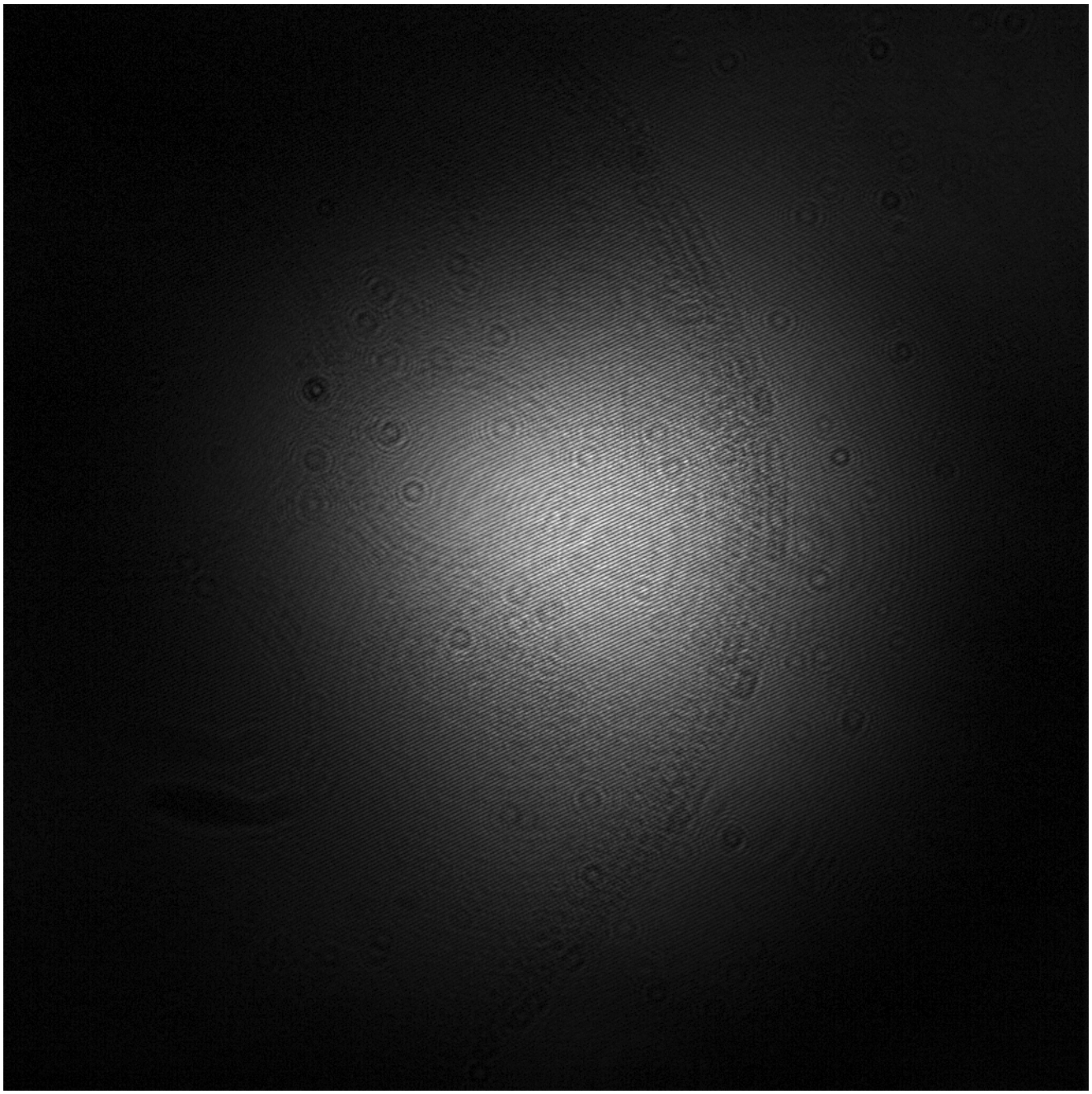

Figure B.3: Diffraction measurement of a sea anemone stem using straight fringe illumination. See section 4.5.2 for reconstruction results.

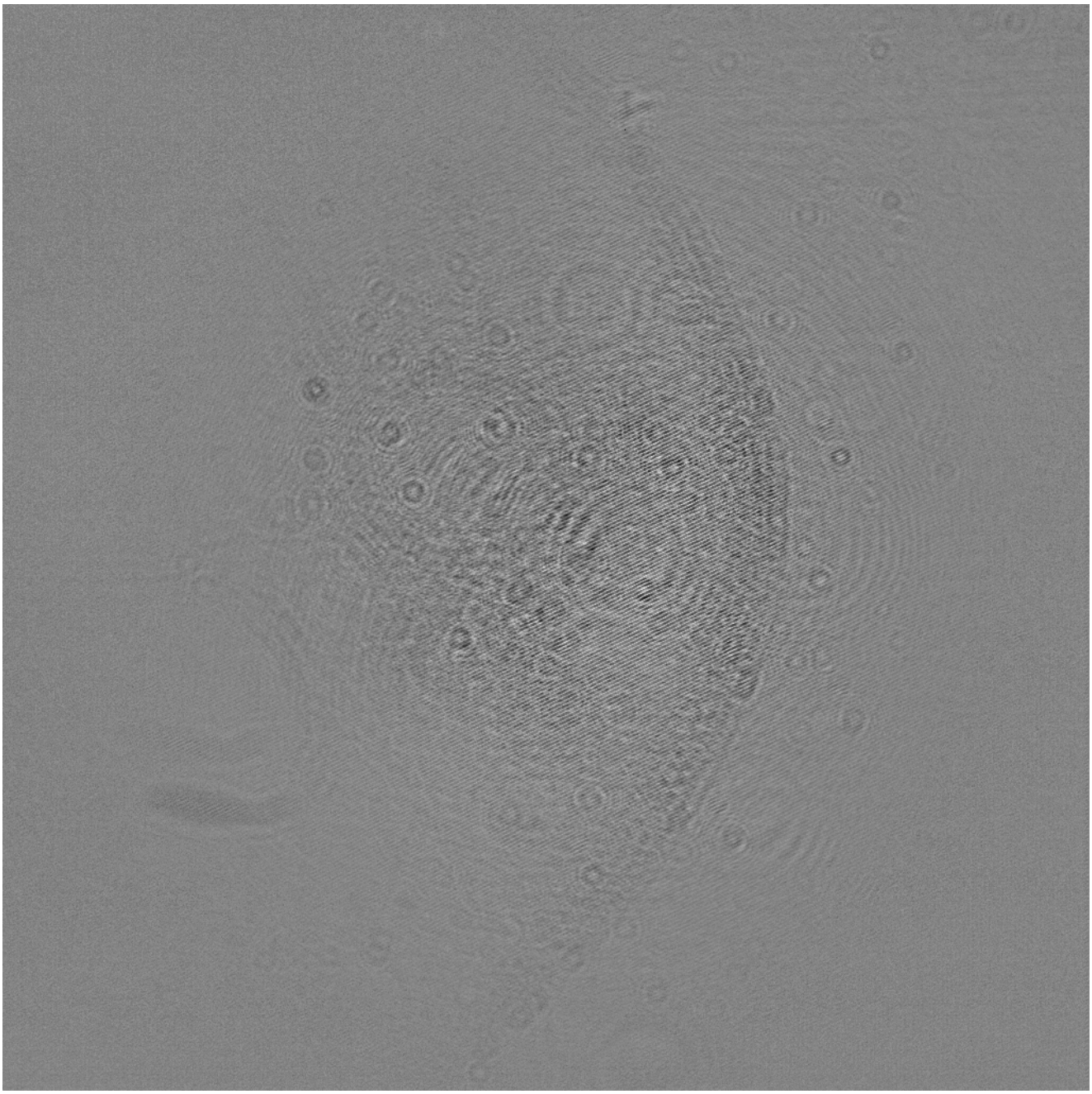

Figure B.4: Difference of reconstructed probe and measured diffraction pattern for a sea anemone stem using straight fringe illumination. The image shows residual fringing in the central part. Reconstruction for this image failed as a result of bad probe reconstruction, see section 4.5.2 for reconstruction results.

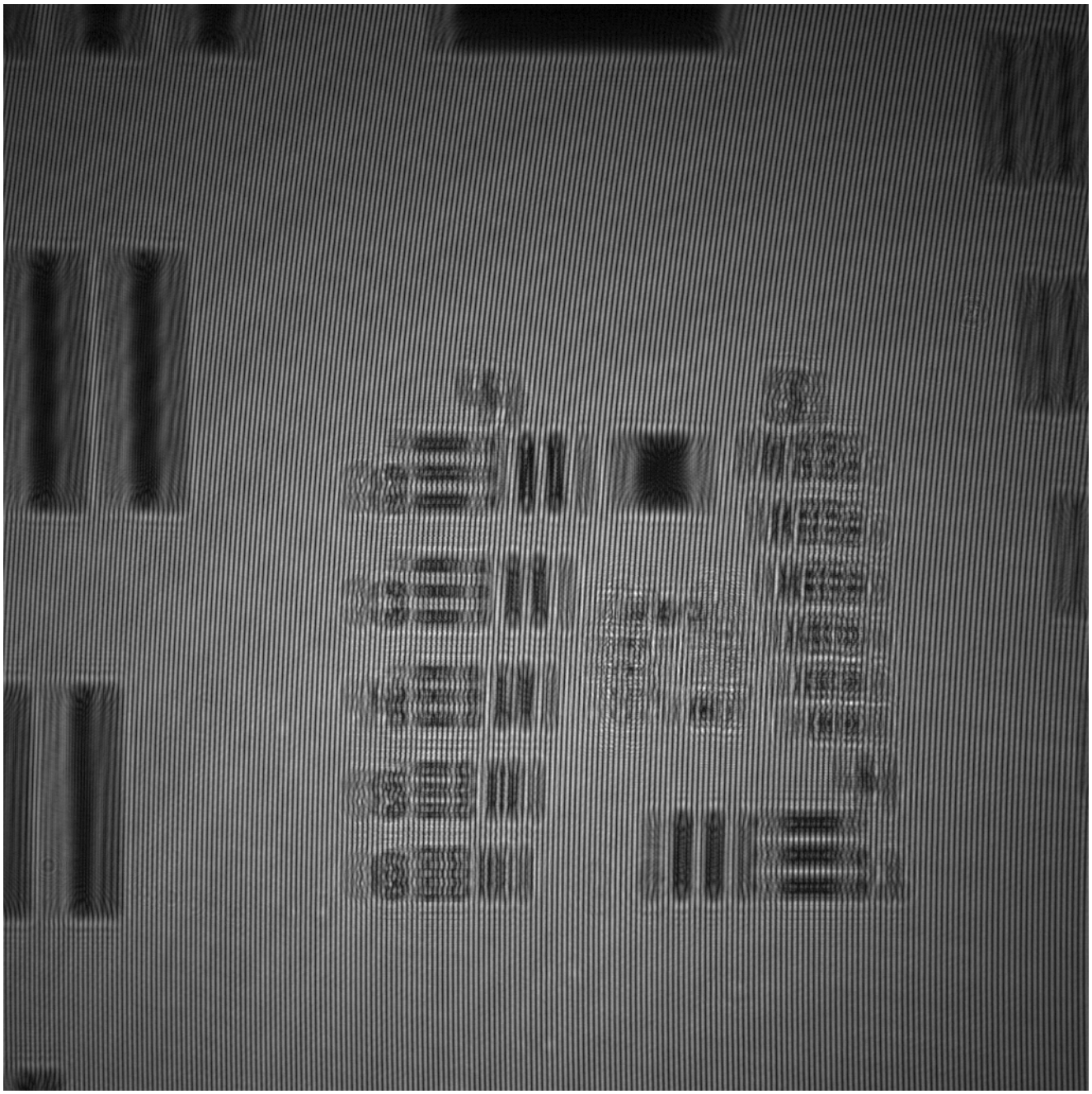

Figure B.5: Diffraction measurement for a usaf 1951 resolution test target using curved illumination. See section 4.6.1 for reconstruction results.

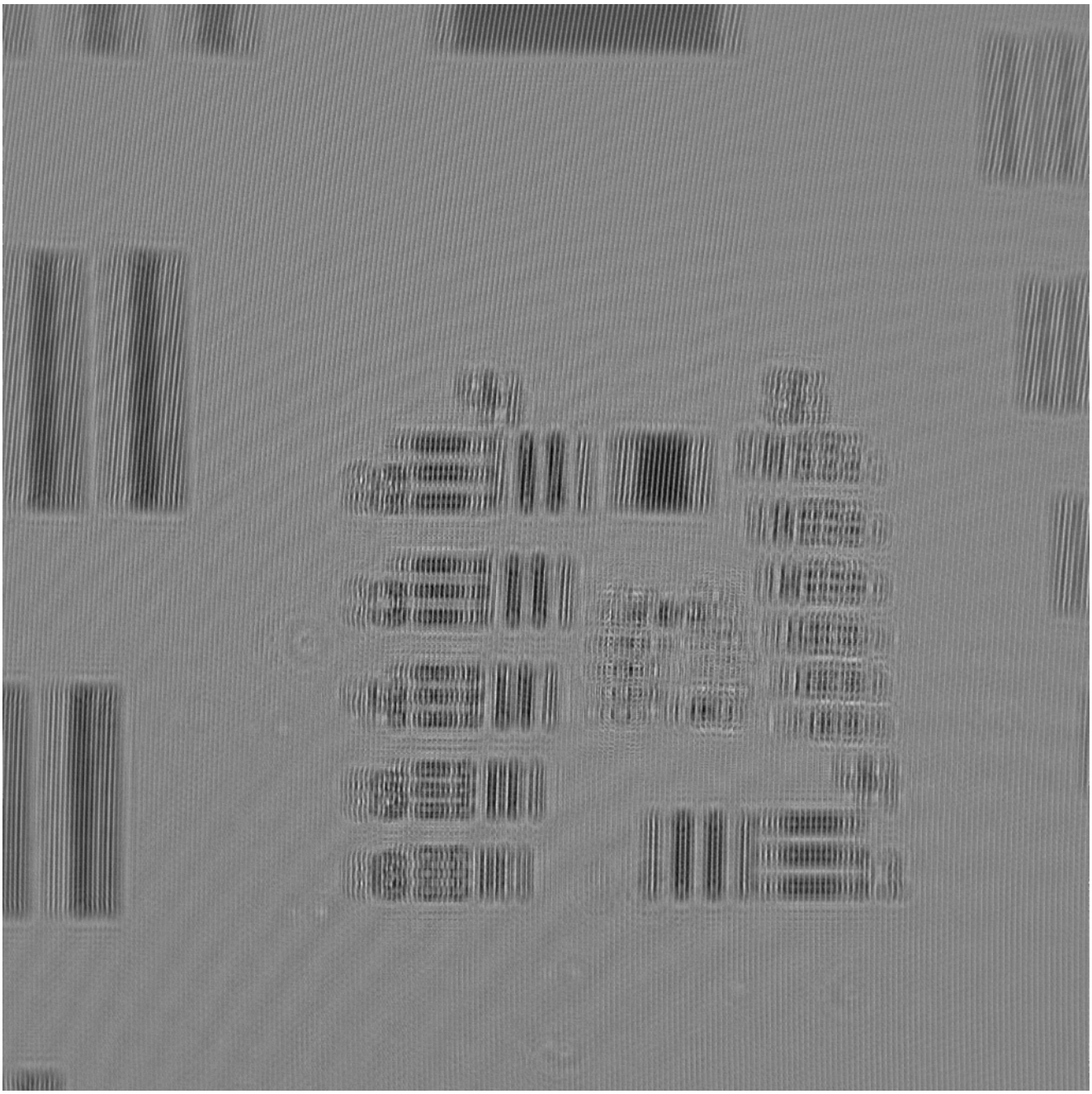

Figure B.6: Difference of the reconstructed probe and measured diffraction using curved fringes. Very little residual fringing remains over the entire domain. The residual signal is recognised as the diffracted objects. See section 4.6.1 for reconstruction results.

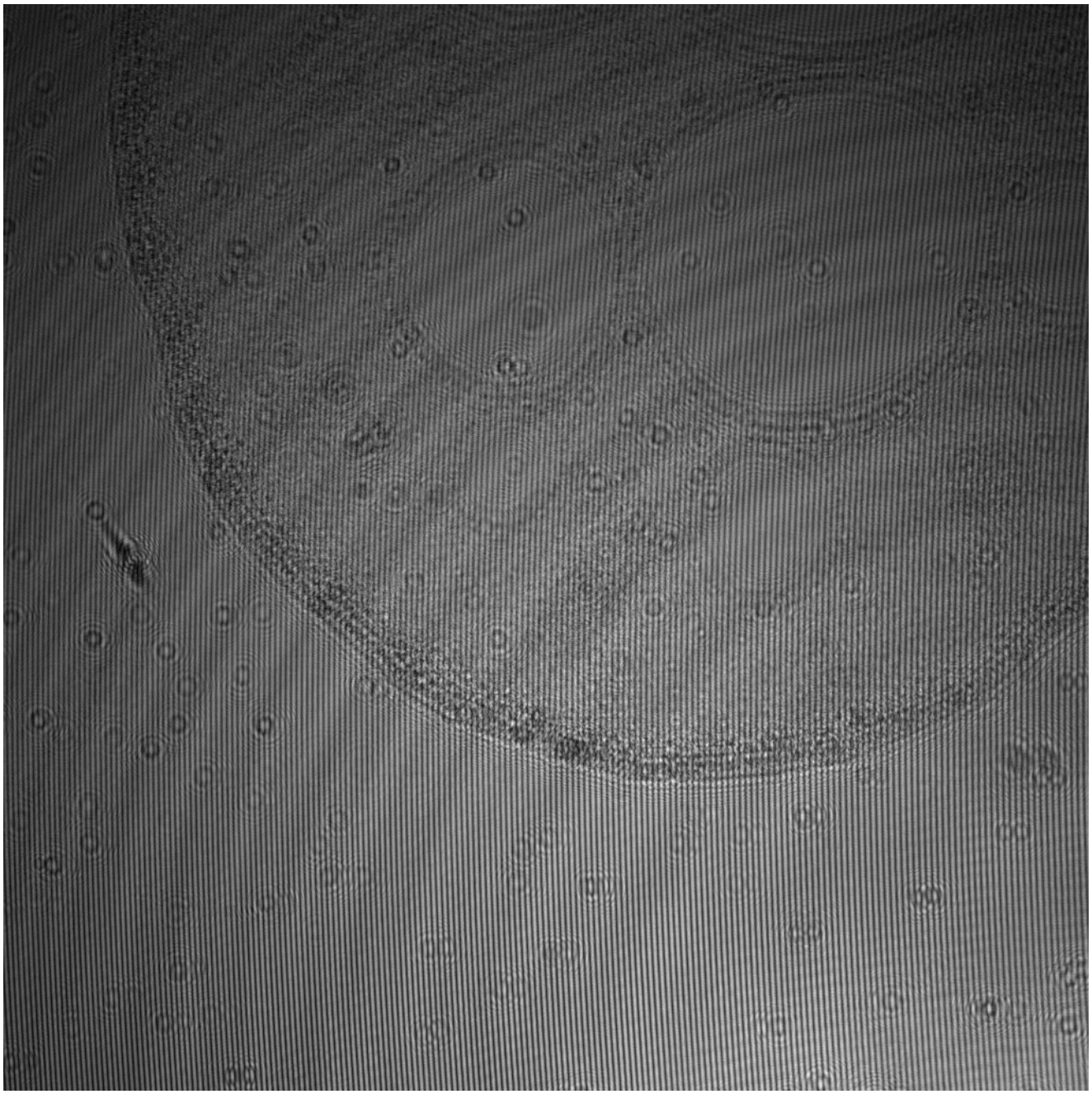

Figure B.7: Diffraction measurement of the stem of a sea anemone using curved fringes. Small circular rings can be recognised after reconstruction as black spots, probably dirt. See section 4.6.2 for reconstruction results.

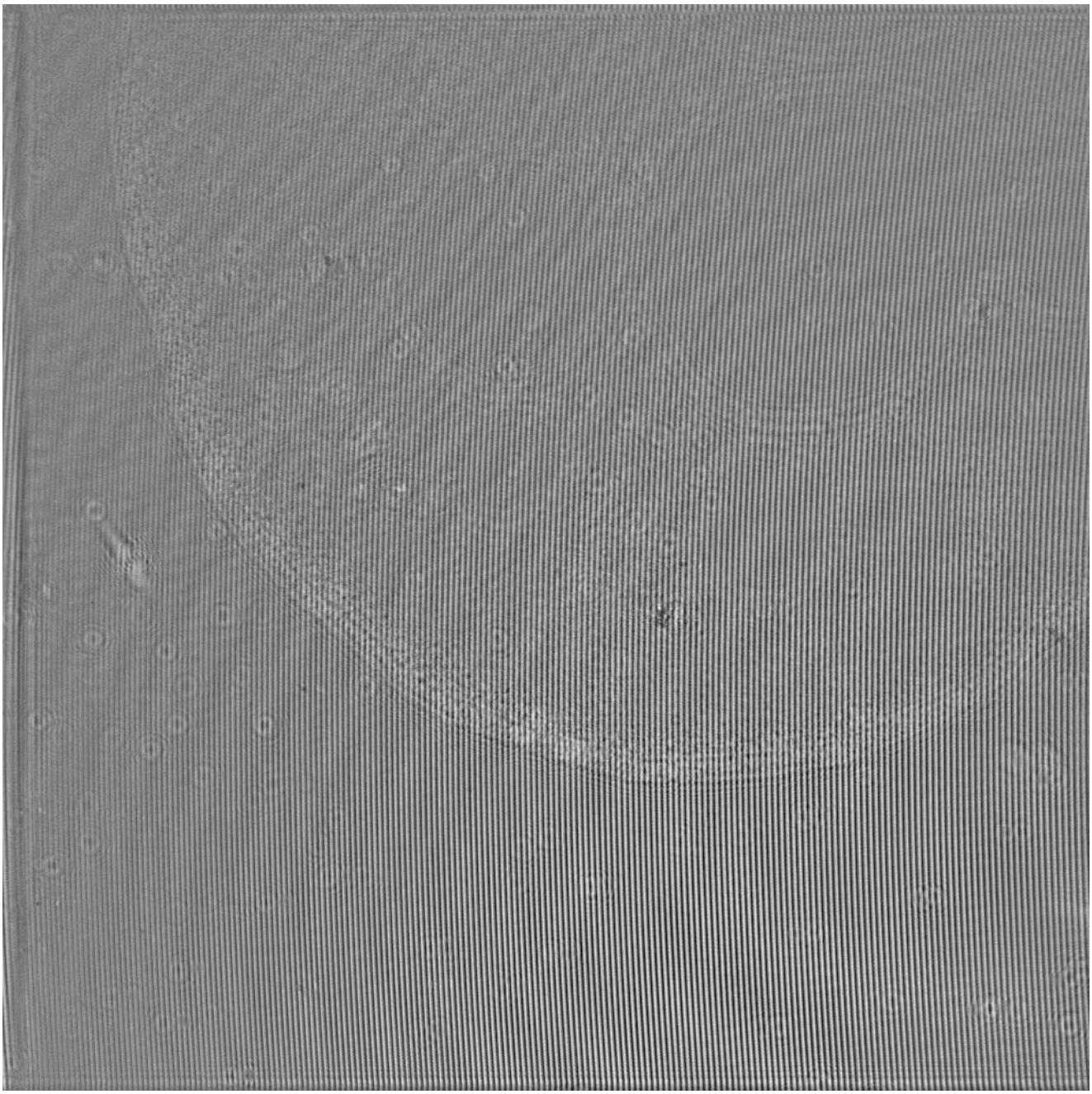

Figure B.8: Difference of reconstructed probe and measured diffraction pattern of a sea anemone stem using curved illumination. The Difference shows a great amount of residual fringing. Surprisingly, image reconstruction was still successful. See section 4.6.2 for reconstruction results and a discussion on the presence of residual fringes.

# Bibliography


[1] Paul Emma, R Akre, J Arthur, R Bionta, C Bostedt, J Bozek, A Brachmann, P Bucksbaum, Ryan Coffee, F-J Decker, et al. First lasing and operation of an ångstrom-wavelength free-electron laser. *nature photonics*, 4(9):641–647, 2010.

[2] M Ferray, A l'Huillier, XF Li, LA Lompre, G Mainfray, and C Manus. Multiple-harmonic conversion of 1064 nm radiation in rare gases. *Journal of Physics B: Atomic, Molecular and Optical Physics*, 21(3):L31, 1988.

[3] James R Fienup. Reconstruction of an object from the modulus of its fourier transform. *Optics letters*, 3(1):27–29, 1978.

[4] RW Gerschberg and WO Saxton. A practical algorithm for the determination of the phase from image and diffraction plane pictures. *Optik*, 35:237, 1972.

[5] JR Fienup and CC Wackerman. Phase-retrieval stagnation problems and solutions. *JOSA A*, 3(11):1897–1907, 1986.

[6] JR Fienup. Phase retrieval using boundary conditions. *JOSA A*, 3(2):284–288, 1986.

[7] Kieran G Larkin and CJR Sheppard. Direct method for phase retrieval from the intensity of cylindrical wave fronts. *JOSA A*, 16(7):1838–1844, 1999.

[8] HML Faulkner and JM Rodenburg. Movable aperture lensless transmission microscopy: a novel phase retrieval algorithm. *Physical review letters*, 93(2):023903, 2004.

[9] John M Rodenburg and Helen ML Faulkner. A phase retrieval algorithm for shifting illumination. *Applied physics letters*, 85(20):4795–4797, 2004.

[10] HML Faulkner and JM Rodenburg. Error tolerance of an iterative phase retrieval algorithm for moveable illumination microscopy. *Ultramicroscopy*, 103(2):153–164, 2005.

[11] Jianwei Miao, Pambos Charalambous, Janos Kirz, and David Sayre. Extending the methodology of x-ray crystallography to allow imaging of micrometre-sized non-crystalline specimens. *Nature*, 400(6742):342–344, 1999.

[12] Ian K Robinson, Ivan A Vartanyants, GJ Williams, MA Pfeifer, and JA Pitney. Reconstruction of the shapes of gold nanocrystals using coherent x-ray diffraction. *Physical review letters*, 87(19):195505, 2001.

[13] David Shapiro, Pierre Thibault, Tobias Beetz, Veit Elser, Malcolm Howells, Chris Jacobsen, Janos Kirz, Enju Lima, Huijie Miao, Aaron M Neiman, et al. Biological imaging by soft x-ray diffraction microscopy. *Proceedings of the National Academy of Sciences*, 102(43):15343–15346, 2005.

[14] Stefan Witte, Vasco T Tenner, Daniel WE Noom, and Kjeld SE Eikema. Lensless diffractive imaging with ultra-broadband table-top sources: from infrared to extreme-ultraviolet wavelengths. *Light: Science and Applications*, 3(3):e163, 2014.

[15] Daniel WE Noom, Dirk E Boonzajer Flaes, Elias Labordus, Kjeld SE Eikema, and Stefan Witte. High-speed multi-wavelength fresnel diffraction imaging. *Optics express*, 22(25):30504–30511, 2014.

[16] JM Rodenburg, AC Hurst, AG Cullis, BR Dobson, F Pfeiffer, O Bunk, C David, K Jefimovs, and I Johnson. Hard-x-ray lensless imaging of extended objects. *Physical review letters*, 98(3):034801, 2007.

[17] GJ Williams, HM Quiney, BB Dhal, CQ Tran, Keith A Nugent, AG Peele, D Paterson, and MD De Jonge. Fresnel coherent diffractive imaging. *Physical review letters*, 97(2):025506, 2006.

[18] Daniel WE Noom, Kjeld SE Eikema, and Stefan Witte. Lensless phase contrast microscopy based on multiwavelength fresnel diffraction. *Optics letters*, 39(2):193–196, 2014.

[19] Joseph W Goodman. *Introduction to Fourier optics*. Roberts and Company Publishers, 2005.

[20] Eric W. Weisstein. Convolution theorem. `http://mathworld.wolfram.com/ConvolutionTheorem.html`. Accessed: 2016-05-09.

[21] Charles Van Loan. *Computational frameworks for the fast Fourier transform*, volume 10. Siam, 1992.

[22] Deepa Kundur and Dimitrios Hatzinakos. Blind image deconvolution. *IEEE signal processing magazine*, 13(3):43–64, 1996.

[23] Gijsbert Michiel Peter Van Kempen. *Image restoration in fluorescence microscopy*. TU Delft, Delft University of Technology, 1999.

[24] CJR Sheppard and A Choudhury. Image formation in the scanning microscope. *Journal of Modern Optics*, 24(10):1051–1073, 1977.

[25] CJR Sheppard, Min Gu, and XQ Mao. Three-dimensional coherent transfer function in a reflection-mode confocal scanning microscope. *Optics communications*, 81(5):281–284, 1991.

[26] Mario Bertero and Patrizia Boccacci. *Introduction to inverse problems in imaging*. CRC press, 1998. Chapter 2.

[27] RW Gerchberg and WO Saxton. Phase retrieval by iterated projections. *Optik*, 35:237, 1972.

[28] S. Hooker and C. Webb. *Laser Physics*. Oxford Master Series in Physics. OUP Oxford, 2010.

[29] Eugene Hecht. *Optics*. Addison-Wesley, 4th international edition edition, 2002.

[30] 1951 usaf resolution test chart. `https://en.wikipedia.org/wiki/1951_USAF_resolution_test_chart`. Accessed: 2016-06-24.

[31] Tony Wilson and Colin Sheppard. *Theory and practice of scanning optical microscopy*, volume 180. Academic Press London, 1984.

[32] Arnaud Dubois, Kate Grieve, Gael Moneron, Romain Lecaque, Laurent Vabre, and Claude Boccara. Ultrahigh-resolution full-field optical coherence tomography. *Applied optics*, 43(14):2874–2883, 2004.

# Index